SAND2000-0264J

Nanostructural Characterization of Amorphous Diamondlike Carbon Films

M. P. Siegal and D. R. Tallant

Sandia National Laboratories, Albuquerque, NM 87185

L. J. Martinez-Miranda

University of Maryland, Department of Materials and Nuclear Engineering

College Park, MD 20742

J. C. Barbour, R. L. Simpson and D. L. Overmyer

Sandia National Laboratories, Albuquerque, NM 87185

ABSTRACT

Nanostructural characterization of amorphous diamondlike carbon (a-C) films grown on silicon using pulsed-laser deposition (PLD) is correlated to both growth energetics and film thickness. Raman spectroscopy and x-ray reflectivity probe both the topological nature of 3- and 4-fold coordinated carbon atom bonding and the topographical clustering of their distributions within a given film. In general, increasing the energetics of PLD growth results in films becoming more "diamondlike", i.e. increasing mass density and decreasing optical absorbance. However, these same properties decrease appreciably with thickness. The topology of carbon atom bonding is different for material near the substrate interface compared to material within the bulk portion of an a-C film. A simple model balancing the energy of residual stress and the free energies of resulting carbon topologies is proposed to provide an explanation of the evolution of topographical bonding clusters in a growing a-C film.

PACS Nos.: 81.05.Tp, 78.30.Na, 61.10.Kw, 61.43.Er

Key words: amorphous carbon, x-ray reflectivity, Raman spectroscopy, density, bonding

Submitted to: Physical Review B1: Inhomogeneous, disordered, and partially ordered systems.

I. INTRODUCTION

Hydrogen-free amorphous diamond-like carbon (a-C) films with properties approaching those of diamond are grown using energetic physical deposition processes, such as ion beam, cathodic filtered arc, or pulsed-laser deposition (PLD).[1-3] These techniques are similar in that each involves the deposition onto a given substrate of small carbon atom or ion clusters ranging from one to several atoms. These methods allow varying degrees of control, as well as different ranges, of the kinetic energy of depositing C species. The energetics of the film growth processes determine the ratio of threefold (sp^2-like) and fourfold (sp^3-like) coordinated carbon atoms. Much of the reported work centers on applications such as hard coatings, and cold-cathode electron emitters for flat-panel displays and vacuum microelectronics.[4-9] The nearly diamondlike tribological properties of a-C films are currently being explored for use in flexural plate wave sensors and as a structural material for microelectromechanical systems (MEMS).[10] Despite this move toward application, there is still much that is not understood about the topology, or nanostructural bonding configurations, within a-C films.

The topography, or distribution, of these bond mixtures is also difficult to measure, given the low atom mass of carbon and the disordered nature of amorphous-C. Theoretical studies can provide insight.[11-20] A level of confidence can be gained by comparing the computational results to experimental radial distribution functions. Two independent first-principles models representative of a-C have shown remarkable agreement to both experiment and to each other.[17,18] The constraint imposed upon each calculation was the assumed density of a given form of a-C, in these cases, ~ 3.0 g/cm^3. In addition, the unit cell was limited to 64 atoms, for the sake of computational time and complexity. Nevertheless, each model suggests that fourfold coordinated carbon atoms exist in distorted ring structures ranging from 3 to 9 units, with 5- and 6-membered rings dominating. Threefold coordinated carbon atoms can exist in conjugated chainlike structures. Conventional threefold coordinated ring structures, while not observed in these

DISCLAIMER

DISCLAIMER

Portions of this document may be illegible in electronic image products. Images are produced from the best available original document.

calculations, cannot be ignored due to the small 64-atom basis sets used in the calculations. A model produced by the reverse Monte-Carlo technique with a much larger basis set of 3000 atoms finds that atoms with 3-fold coordinated bonds tend to form both small clusters and conjugated chains interlinking regions of the dominant 4-fold coordinated carbon atoms.[19] A recent first-principles structural model of the surface region of a-C, which is believed to have a significantly higher 3-fold coordinated carbon atom presence than the bulk, clearly identifies the presence of both planar rings and chains.[20]

Most studies assume that a-C is homogeneous, with representations such as those described above, throughout the thickness of a given film. We demonstrated that this is not the case in a recent high-resolution transmission electron microscopy (HRTEM) study of films grown by PLD using different deposition energetics.[21] Similar results were also reported for a-C films grown using the filtered cathodic arc and studied using spatially-resolved cross-sectional electron energy loss spectroscopy.[22] A minimum of three distinct layers were found: relatively low-density layers at the film/surface and film/substrate interfaces, and a higher density bulk component of the film in the middle. The density is assumed to be a direct result of the ratio of three-to-fourfold coordinated carbons in a given portion of the material. However, the film structure is even more complex; the bulk component appears to have a monotonically decreasing density gradient with its distance from the interface. In addition, the thicknesses of the surface and interface layers increase with deposition energy. These structural features are explained in terms of the energetics of the depositing specie on a solid surface, in analogy to ion beam – solid interactions.

This combination of recent computational and nanostructural experiments is making the topology (geometric bonding structures) and topography (distribution of bonding structures) of a-C materials more clear.[17-20, 23] Representative topologies of energetically favorable threefold and fourfold coordinated carbon atom clusters now exist, and their distribution within a given film is known to be inhomogeneous. However, we do not know how, and if, the local topologies are

impacted as the ratio of the two coordinated forms of carbon atoms changes within a given film. This paper will attempt to provide insight to this issue, fundamental to developing a detailed description of a-C films at the local bonding level. We use Raman spectroscopy to provide optical property measurements and information about the bonding nature of the threefold coordinated carbon atoms, and x-ray reflectivity (XRR) measurements to look at variations of material density, both as functions of the deposition energetics and film thickness (or distance from the film/substrate interface).

II. EXPERIMENT

We use 248 nm radiation from a KrF excimer laser to ablate carbon species from a pyrolytic graphite target in a vacuum chamber with base pressure < 10^{-7} Torr. Carbon deposits onto rotating Si (100) substrates maintained at ambient temperature (below 50 °C). The target-to-substrate distance is ~ 5 inches. The rotating target is positioned slightly off-axis from the central portion of the plume, allowing uniform a-C film growth on substrates up to 4 inches in diameter, significantly wider than the 2" diameter substrates typically used. Laser pulses (duration ~ 17 ns) are focussed on to a rectangular spot off the center of the rotating pyrolytic graphite target to prevent excessive cratering with an area ~ 0.01 cm^2. A 10 Hz repetitiion rate is typically used. The threefold to fourfold coordinated C atom ratio is controlled by varying the laser energy density ablating the graphite target.[24-26] A small portion of the substrate was usually masked off during a-C film growth in order to have a sharp step for thickness and optical property measurements. Three sets of a-C films were prepared for the experiments presented in this paper. First, in order to study the effect of laser energy density on resulting a-C film structures, we grew a set of films nominally 100 nm thick where we varied the laser energy density from 5 to 125 J/cm^2. Second, we grew a set of films at a constant laser energy density of 45 J/cm^2 with thicknesses ranging from 5 – 200 nm to study variations in film properties as a function of distance from the film/substrate interface. Third, we grew 7 nm thick a-C films simulataneously onto both bare Si(100) and ~ 20 nm thick

tungsten-coated Si(100) using a relatively high laser energy density of ~ 40 J/cm^2 to determine the potential presence of Si-C bond formation at the interface and its effect on our measurements.

We investigated the compositional purity of the a-C samples using Rutherford backscattering spectrometry (RBS) and elastic recoil detection analysis. No evidence is found for any significant impurity concentrations to 0.01 atomic % levels, with the exception of a layer of hydrogen atoms near the film/substrate interface. Typically these films have about 0.8 atomic percent H at this interface, most likely a residue from the HF Si-substrate cleaning procedure used prior to film growth. Such a small percentage of H at this interface is unlikely to greatly affect the local bonding geometries, especially considering that hydrogenated diamondlike carbon films grown by chemical vapor deposition methods typically consist of greater than 20 atomic percent H.

Film thickness is nominally measured using a stylus profilometer. Raman spectra are obtained using a triple spectrograph operated, with a liquid-nitrogen cooled charge-coupled detector, at 6 cm^{-1} resolution. Raman scatter is excited using the 514.5 nm wavelength (green light) of an argon ion laser. Measurements are made both on the film and on the bare Si substrate exposed during film growth to determine optical transparency. We infer film density using x-ray reflectivity (XRR), performed at the National Synchrotron Light Source (Brookhaven National Laboratory), beamline X22A, using 1.20373 Å (10.3 keV) x-rays. The experimental full width half maximum resolution, achieved with a Si(111) monochromator and Si(111) analyzer, is $\Delta E/E \sim 1 \times 10^{-4}$.

Raman spectroscopy easily discerns the difference between elemental forms of carbon.[27] Crystalline diamond has a narrow Raman band peaking at 1332 cm^{-1}. Graphite has two significant Raman bands. The first is due to a Brillouin-zone-center phonon at 1578 cm^{-1}. The second band peaks at 1365 cm^{-1} and is from a zone-edge phonon that becomes symmetry-allowed in the reduced symmetry environment at the edges of graphite crystals.[28] The intensity of graphite Raman

bands are enhanced with visible excitation by the interaction of electronic ($\pi \rightarrow \pi^*$) transitions with vibrational transitions, such that Raman spectra of nanometer thicknesses of graphite are easily obtained.[29] Diamond Raman bands do not experience resonance enhancement with visible excitation, since vacuum ultraviolet wavelengths are required to access the ($\sigma \rightarrow \sigma^*$) electronic transitions of diamond. Therefore, vibrational bands from the threefold coordinated (π-bonded) carbon structures dominate the Raman spectra of amorphous carbon materials containing both forms of carbon when visible wavelengths are used for excitation. Raman spectra using visible light excitation indirectly provide information concerning the relative proportion of π- and σ-bonded carbon due to its detection of a signal from the Si substrate material, the intensity of which is directly related to the optical transparency of the a-C film, i.e. its diamondlike nature.

XRR spectra are collected near the critical angle of total reflectivity and are fit to the Fresnel interference equations which describe optical reflectivity. In general, film density is related to the critical angle of total reflectivity by:

$$\alpha_c^2 = \frac{(e^2\lambda^2)}{\pi mc^2}\frac{(\rho Z)}{A}N_0 \qquad (1)$$

where α_c is the critical angle, N_0 is Avogadro's number, Z is the average atomic number, A is the average atomic mass, ρ is the mass density of the sample, and λ is the x-ray wavelength.[30-32] However, analysis of XRR spectra becomes more complicated when the material under study is not uniform or exists in layers. This is precisely the case as shown in our study using HRTEM.[21] At least three distinct and inhomogeneous layers exist within a-C films resulting from the energetics of the growth process. Hence, a full analysis of XRR spectra should include information about each layer (composition, density, gradients and thickness), surface and interface roughnesses, and the intensity and position of any small-angle Bragg diffraction peaks arising due to a long-range periodicity. These details will be presented elsewhere in a more complete description of the use of XRR for the study of a-C films.[33] For the purposes presented in this paper, we assume to first-order that the critical angle of reflection is dominated by the highest

density material within the penetration length of the x-rays used. Comparisons will be made with the accurate density measurements in ref 21 using the same films to provide confidence in the use of XRR for the determination of density. The earlier study used RBS to measure the C atom areal density and HRTEM to measure film thickness. Density is then precisely the ratio of these two measureables.

III. RESULTS

A. Raman spectroscopy

Figure 1 shows normalized Raman spectra, scaled to C band maximum intensity, for ~ 100 nm thick a-C films grown with laser energy densities ranging from 5 to 125 J/cm^2. The flat-topped feature occurring between 925 and 1025 cm^{-1} is a second-order phonon band from the silicon substrate. Note that the intensity of this band increases with increasing PLD growth energy, demonstrating that the films become more transparent, or diamond-like. This implies an increase in the four-to-threefold coordinated carbon atom ratio in a-C as a function of PLD growth energetics. The broad band between 1050 and 1800 cm^{-1} and centered near 1550 cm^{-1} is due to resonantly-enhanced vibrational modes of 3-fold coordinated carbon. The C bands tend to narrow and shift to higher frequency with increasing deposition energy. As discussed earlier, this band is composed of resonantly enhanced vibrations from π-bonded carbon atom pairs found in either chains or ring structures with different vibrational frequencies. Therefore, a systematic shift of the peak position suggests a change in the composition of such 3-fold coordinated carbon atom clusters. We consider this later in the discussion section. Prior to normalization (not shown), the integrated intensity of this broad band also decreases as the PLD growth energy increases. These trends are associated with a decrease in π-bonded structures in films grown with increasing PLD energy density, consistent with the increase in optical transparency. Raman scatter from fourfold coordinated carbon atom bonds, those exhibiting σ-like hybridization, occurs below the crystalline diamond vibrational frequency of 1330 cm^{-1}. However, due to the lack of resonant-enhancement, Raman scatter from σ-bonding cannot be observed in the presence of π-bonds. Raman scattering

using ultraviolet radiation reduces the resonant-enhancement from π-bonds and was recently shown to be an effective tool for studying σ-bonds.[5, 29, 34-36]

Optical transparency at 514.5 nm is determined by measuring the integrated intensity of the Si band through an a-C film and from a bare Si region on the same sample that was masked during a-C film growth. The ratio of these intensities is the transparency, T, through twice the thickness of the film, since the Raman measurement is in reflection mode. We made this measurement for both the major Si Raman band (from 480 – 560 cm^{-1}) and for the second-order phonon (925 – 1025 cm^{-1}). This is shown in fig. 2(a). Both Si Raman bands exhibit identical behavior for optical transparency at 514.5 nm. As expected, transparency improves monotonically with PLD growth energy, suggesting increased diamondlike properties. The absorbance, determined using data from both Si bands, is then simply the $\log_{10}$ (T^{-1}) and is shown in figure 2(b) as a function of PLD growth energy for 100 nm thick films. Note that the absorbance of green light in a-C films decreases nearly exponentially with the PLD energy density used for growth.

Our previous HRTEM study clearly found that a-C films are not uniform in mass density perpendicular to the substrate.[21] Indeed, with the exception of fixed interface and surface regions for a given growth energy, the bulk portion of a film appears to have a density gradient that decreases with distance from the substrate. The extent of this gradient is a function of the growth conditions. The presence of a gradient implies a change in the fraction of fourfold versus threefold coordinated carbon atoms. However, it is not known how the local topologies, or bonding configurations, vary as the ratio of these clusters change. Figure 3 shows normalized Raman spectra, again scaled to the C band intensity, for the second set of films grown at a constant 45 J/cm^2 at thicknesses ranging from 5 to 200 nm. Not surprisingly, the response from the Si substrate is very large for the thinnest films studied. The intensity from the Si band clearly decreases with increasing film thickness. However, the shape and position of the carbon Raman bands also changes with film thickness. Such changes are associated with variations in the

composition of the threefold coordinated carbon clusters embedded in these films. Again, there is a monotonic shift of the peak position with film thickness suggesting changes in the threefold coordinated carbon bonding topology.

Figure 4(a) plots the Raman optical transparency for a-C films grown as a function of thickness at constant energy. The transparency actually increases with film thickness from 5 to 20 nm, suggesting an increase in the diamondlike nature of carbon bonding in these films with increasing thickness. A previous study found that the combined thickness of the interface and surface layers alone is about 20 nm for films grown at 45 J/cm^2.[21] Therefore, these two layers are still developing for films with total thickness $\leq$ 20 nm. The transparency then falls off exponentially with increasing film thickness beyond 20 nm. Optical absorbance is plotted in fig. 4(b), exhibiting different linear behaviors over two ranges of film thickness. The low absorbance for the thinnest films is consistent with a very high fourfold coordinated, or diamondlike, carbon content within the films. As film thickness grows beyond 20 nm, a bulklike region of the films develop. The absorbance for a-C films $\geq$ 20 nm increases linearly, suggesting the presence of a growing region that is less diamondlike in nature. These trends are shown more dramatically by normalizing the absorbance with film thickness. This results in the plot of optical absorption coefficients, shown in fig. 4(c). Here we observe the large exponential increase in diamondlike bonding with increasing film thickness from 5 – 20 nm, or to the thickness of the fully developed surface and interface layers. The slight logarithmic increase in the absorption coefficient for increasing film thicknesses up to 200 nm suggests a gradient in carbon bond types. The a-C samples with the lowest determined absorption coefficients are the 20 nm thick films where the interface and surface regions are fully developed. The absorption coefficient values of 3500 – 5750 cm^{-1} are a factor of ten greater than the 490 cm^{-1} measured from fine-grained diamond films grown by microwave plasma-assisted chemical vapor deposition.[37]

We provide a detailed interpretation of these Raman spectra in the discussion section. Pertinent to such discussion is the effect of any Si-C bonding at the interface. It has been reported elsewhere that there is a Si-Si Raman vibration in a-SiC at 1445 cm^{-1}, which is well within the C band in our Raman spectra.[38] We grew two thin (~ 7 nm) a-C films simultaneously, one on a bare Si substrate, and one on a tungsten-coated silicon substrate. The Raman spectra for these films are shown in fig. 5. The spectra with the more narrow C band is from the film grown on W. The difference spectrum clearly shows the presence of a small peak at 1445 cm^{-1}, consistent with interfacial Si-C bonding. However, the contribution from this vibrational frequency is small; we deem its presence inconsequential for interpreting the Raman spectra from films of this and the greater thicknesses presented in this paper.

B. X-ray reflectivity

The XRR spectra from a-C films nominally 50 nm thick grown with laser energy densities of 11, 27 and 45 J/cm^2 are shown in fig. 6.[39] These are the identical films studied by RBS and HRTEM presented in ref. 21. A simple analysis of the oscillation widths from these XRR spectra assuming a single layer a-C film yields thickness determinations of 39, 49 and 57 nm, respectively. This is in good agreement with the 43, 52, and 58 nm thicknesses measured via HRTEM. The small differences are likely the result of not fully fitting the XRR data with the three distinct layers of carbon observed in the HRTEM micrographs.

These spectra also show gaussian Bragg scattering peaks, marked with arrows, near 2θ = 0.9° for the 11 J/cm^2 film (curve a), and near 2θ = 0.5° for the 27 and 45 J/cm^2 films (curves b and c, respectively). These small angle peaks relate to a quasi-periodic array of scattering sites spaced 8 to 15 nm apart. These scattering sites must represent structure(s) that may be located at the film/substrate interface, within the film, or at the film surface. The layer thicknesses determined from HRTEM do not correlate with these values.[21] Another possibility is the quasi-periodicity

of surface and/or interface roughness. Further work is required for positive identification of the source of the Bragg scattering peaks.[33]

To first order, film density is related to the critical angle of reflection through equation (1). Note that the intensities measured at the critical angle in fig. 6 do not experience a sharp drop, but rather a more gradual decrease. This effect can be related to the presence of a density gradient near the surface of the films, consistent with the HRTEM images in ref. 21. We use the angle with the absolute sharpest drop in reflected intensity to estimate the highest density present near the surface region. This will be discussed further below. The extracted densities of these nominally 50 nm thick films (closed circles) increase with increasing growth energetics and are plotted in fig. 7. This is consistent with an increasing ratio of 4-fold coordinated carbon atoms. These values compare favorably to the densities measured for these same films by RBS and HRTEM (open circles). The greatest variation is for the film grown at the lowest PLD energy density. Such low deposition energies blur the boundaries between the interface and surface layers with the bulk layer. Hence, it is possible that the critical angle of this film is related to an average density of the surface and bulk regions. The average mass density for all regions of this film was measured by RBS/HRTEM to be 3.06 g/cm^3, which is close to the XRR fitted value of 3.0 g/cm^3.[21]

While densities of 3.35 g/cm^3 for highly diamondlike a-C, as seen in fig. 7 for 50 nm thick films grown at 45 J/cm^2, are considerably higher than the typical average density of ~ 3.0 g/cm^3 reported elsewhere,[24, 35, 40-44] we now arrive at such values using two completely independent methods of measurement.[21] Note that the densities of crystalline diamond and graphite are 3.51 and 2.25 g/cm^3, respectively. The density of glassy carbon, or nanocrystalline graphite can be as low as 1.8 g/cm^3. Since simple packing rules dictate that pure amorphous diamond must be less dense than crystalline diamond, it is not possible to calculate the precise four to threefold coordinated C atom ratio based on a linear interpolation of density using the values for

both graphite and diamond. Such a simple calculation can lead only to a minimum fourfold coordinated carbon fraction ≥ 87 %.

The densities, determined by XRR, of 100 nm thick films grown at the same set of PLD energy densities, are also shown in fig. 7. There are two important points. First, the density values are significantly lower than those for the thinner films. This result is consistent with HRTEM images showing a density gradient in the bulk portion of the films.[21] Hence, thick films have a lower density within the portion of the bulk layer closest to the surface layer than thinner films. We explore this in greater detail below. Second, the density varies little for 100 nm thick films grown at 27 and 45 J/cm^2. This latter observation suggests either a lower limit on the energy density dependence for atomic density, or a saturation of energy fluence to create a given atomic density.

Figure 8 shows the densities determined using XRR from the films with varying thickness grown at 45 J/cm^2 characterized by Raman spectroscopy shown in fig. 3. The mass density is high, near 3.35 g/cm^3 for films thicknesses up to 50 nm. The density begins to drop off above this thickness. The density for 100 nm thick films is ~ 3.0 g/cm^3. The density continues to decrease with film thickness. Films cannot be grown significantly thicker than 200 nm due to the accumulation of residual stress resulting in spallation. The density of 200 nm thick films is found to be ~ 2.55 g/cm^3. It is highly unlikely that this represents the average density of the whole film, but rather that of the region near the surface.

IV. DISCUSSION

We can gain greater insight to the structure of a-C films with a better understanding of the mass densities determined using XRR. Above the critical angle of total internal reflection, x-rays penetrate into a given material surface. This penetration depth can be calculated for carbon as a function of density and x-ray incident wavelength, as well as the absorption coefficient of the

material at a specific wavelength.[45]. This is true even for light elements such as carbon. Therefore, the critical angle is not strictly a measure of the bulk density of the material, but of the density of the absorption-controlled penetration depth within the sample. The penetration depth, D, is given by:

$$D = \frac{\lambda}{4\pi q} \tag{2}$$

where $$q^2 = \frac{(\alpha_c^2 - \alpha_i^2) + \sqrt{(\alpha_c^2 - \alpha_i^2)^2 + 4\beta^2}}{2} \tag{3}$$

and, where $$\beta = \frac{\lambda\mu}{4\pi} \tag{4}$$

λ is the x-ray wavelength, α_c is the critical angle, α_i is the incident angle, and μ is the linear absorption coefficient in cm^{-1}. Penetration depth as a function of incident angle is shown in fig. 9(a) for each of the thickness samples measured. Note that below the critical angle the penetration depth for each sample is negligible. The penetration depth increases dramatically at the critical angle for each a-C density, with the point of increase occuring at higher incident angles for films with higher densities. The point of inflection of each curve is used to determine the penetration depth at the critical angle for each sample. Therefore, fig. 9(b) shows the penetration depth as a function of density, measured just above the critical angle, or just at the point where the reflectivity curve suddenly decreases in intensity. Penetration depth increases with decreasing density, or presumably, with an increasing 3-fold coordinated carbon fraction.

The thickness of the surface region of a-C films grown using a PLD energy 45 J/cm^2 is ~ 10 nm, with a density ~ 2.5 g/cm^3, measured by RBS and HRTEM.[21] The x-ray penetration depth at the critical angle for this carbon density is ~ 55 nm, significantly thicker than the surface layer. In fact, it is the high density bulk portion of the films that limits the penetration depth to ~ 22 nm. Therefore, the XRR fitted density of ~ 3.35 g/cm^3 for films with thicknesses $\leq$ 50 nm represents

the bulk portion of the films and is in excellent agreement with the density measurements made using RBS and HRTEM. As the film thickness increases above 50 nm, the density decreases and the penetration length increases further. For the 100 nm thick films, the value of 3.0 g/cm^3 represents the density of the upper 35 – 40 nm of the bulk portion. Finally, the low density of 2.55 g/cm^3 found for the 200 nm thick sample represents the upper 50 – 60 nm of the bulk portion of the film. To a limited degree, the a-C density vs. film thickness graph in fig. 8 represents a depth profile projection of a-C films, excluding the presence of the 10 nm interface and surface layers.

The Raman spectra can also be further characterized by deconvoluting the carbon band of each spectrum into representative vibrational frequencies that are expressed as gaussians. An earlier paper described a similar procedure for the fitting of a-C spectra into two contributions based on the active vibrational modes of disordered nanocrystalline graphite, or glassy carbon, at 1350 (D-mode) and 1581 (G-mode) cm^{-1}.[46] The G-mode Raman band is the only band observed in single crystal graphite and is assigned to a doubly degenerate deformation vibration of the hexagonal ring corresponding to the E_{2g} mode of graphite.[47] The D-mode Raman band is observed in disordered graphite systems and is attributed to either crystalline size [48] or, more generally, to the density of crystalline edges within a sample.[28] In nanocrystalline graphite, the intensity ratio of the D and G bands is related to the average crystal diameter in the graphite plane measured by X-ray diffraction methods.[47, 48] However, no such x-ray peaks have ever been observed for diamondlike a-C films, suggesting that other assignments of the Raman spectra may be appropriate. In addition, in order to achieve a good 'fit' to the spectra, the D and G bands must usually be assigned a frequency of vibration different from that observed in nanocrystalline graphite. Furthermore, these positional assignments vary from film to film, presumably dependent upon the 3-fold to 4-fold coordinated carbon atom ratio.

This paper will present a detailed analysis considering possible vibrational modes based upon

physical characteristics suggested by Doyle and Dennison.[49] As stated above, the contribution to the observed Raman band is solely from threefold coordinated carbon atoms. One possibility is that these atoms are assembled into chain-like clusters which have conjugated π-bonding. This is supported by theoretical computations [17-20, 23] and by analysis of electronic transport measurements.[50-51] The latter work suggests an average chain containing 12-13 atoms to account for the conductivity in films grown with a PLD energy of 45 J/cm^2. For example, polyvinyl chloride (PVC) is a polymer which spontaneously generates conjugated polyene chains following thermal degradation. Raman spectra of degraded PVC show resonance enhancement with green excitation wavelengths of bands from conjugated chains reaching about 34 carbon atoms in length.[52] The spectra consist of two relatively narrow bands, with ~ 30 cm^{-1} bandwidth, of nearly equal intensity peak about 1100 and 1500 cm^{-1}. Such bands cannot account for the Raman spectra in figs. 1 and 3. This is not to state that such chain-like structures do not exist in a-C. It is more likely that the density of such structures is small, or its resonance enhancement from 514.5 nm excitation is not as strong, compared with other threefold coordinated carbon structures.

Another possible set of structures incorporate threefold coordinated carbon atoms into sheets of π-bonded rings. While 6-membered ring topologies are the most stable (graphene structures), rings of other sizes are possible in solid-state materials. For example, fullerenes and nanotubes include 5- and 7-membered rings, in addition to 6-membered carbon rings, to impart curvature. The limited size of the basis sets used in the first-principles computations are simply too small to provide evidence of all existing structures, especially within the minority π-bonded subset. However, a less-precise model, with a much larger basis set, finds that atoms with threefold coordinated bonds tend to form both small clusters and conjugated chains.[19] Additionally, a recent first-principles structural model of the surface region of a-C clearly identifies the presence of both planar rings and chains.[20]

The Raman frequencies of idealized 5-, 6-, and 7-membered π-bonded carbon rings have been calculated theoretically by Doyle and Dennison.[49] While idealized ring structures are unlikely to occur in highly-strained a-C materials, vibrational shifts due to ring distortions act mainly to broaden the range of frequencies rather than to significantly shift the average vibrational frequency for a given ring structure. Both breathing (A-type) and stretching (E-type) symmetry modes for each numbered carbon ring structure exist with vibrational frequencies within the Raman bands measured for our a-C films. Given that the presence of threefold coordinated carbon atoms is minimized in films grown at our highest energy conditions, it is likely that cluster sizes of such rings are also minimized. Since 6-membered C rings are the most thermodynamically stable π-bonded structure, we fit the spectra from the a-C film grown at 125 J/cm^2 using only A_{1g} at 1360 cm^{-1} and E_{2g} at 1569 cm^{-1} for 6-membered C atom rings. The high-quality of such a simple fit is shown in fig. 10(a). We use the parameters of this fit to fix the characteristics of these two vibrational modes relative to one another for analyzing the spectra from the remaining less diamondlike films. We find that the intensity of the E_{2g} is 8.2 times greater than that of the A_{1g} mode, while the A_{1g} bandwidth is 1.5 times greater than the E_{2g}. In Doyle and Dennison's calculations, both vibrations are intrinsic to individual rings and are allowed transitions.[49] In clustered 6-membered rings, the A_{1g} becomes less allowed due to symmetry.[53]

For a-C films with an increased fraction of 3-fold coordinated carbon atoms, a greater degree of π-bonded ring clustering is likely to form. As discussed above, the highly strained environment within these a-C films will force curvature in these clusters, resulting in the evolution of both 5- and 7- membered carbon rings. Since 5- and 7-membered rings lack inversion symmetry, the A modes dominate. In summary, the symmetry modes relevant to our range of collected data are A_{1g} at 1360 cm^{-1} and E_{2g} at 1569 cm^{-1} for 6 C-atom rings, A_1. at 1444 cm^{-1} for 5 C-atom rings, and A_1. at 1303 cm^{-1} for 7 C-atom rings.[49]

We can fit all of our Raman spectra with gaussians centered around these frequencies. The

only adjustable parameters used are the intensity and bandwidth of each gaussian, with the exception that the relative intensites and bandwidths of the two 6-membered carbon ring vibrations are fixed. We find that all the fitted bandwidths range from 90 – 250 cm^{-1}. Figure 10(b) shows the quality of the fit using all four frequencies for the a-C film grown using the lowest energy, 5 J/cm^2.

Figure 11 shows the fractional contribution of each vibrational frequency to the entire threefold coordinated C portion of the Raman spectra as a function of PLD growth energy. For films grown at the lowest energy densities, contributions from all four vibrations are apparent, with nearly equal weighting given to those from 5-, 6-, and 7-membered C ring structures. As the PLD growth energy density increases, films contain a smaller fraction of threefold coordinated atoms leading to a preponderance of 6-membered ring structures. Interestingly, the curves used to fit the data in fig. 10 show a logarithmic increase of 6-membered ring structures and an exponential decrease of 5- and 7-membered ring structures as a function of increasing growth energy. In general, it appears that isolated flat sheets of 6-membered rings are favored as the overall population of threefold coordinated C atoms decreases with increasing growth energy, with the resulting threefold nanostructures becoming smaller and more isolated. At low growth energies, with a higher proportion of threefold coordinated carbon atoms, such structures are likely to be larger and more densely packed, resulting in the incorporation of 5- and 7-membered rings, similar to fullerene structures, to impart curvature to their surfaces. This behavior can be rationalized by considering the alternative to an increase in the proportion of 5- and 7-membered rings with increasing 3-fold coordinated carbon. Sheets of (flat) six-membered rings present in high density would be expected to stack, forming graphite-like structures with crystallinity on the nanoscale. However, neither the Raman band pattern nor the x-ray diffraction pattern characteristic of nanocrystalline graphite has been observed in these films. In summary, analysis of the Raman spectra suggest that the threefold coordinated portion of a-C films become dominated by six-membered C rings as the overall fraction of π-bonded carbon atoms decreases.

The Raman spectra measured as a function of film thickness at a constant PLD growth energy density of 45 J/cm^2 can be deconvoluted in a similar manner. Figure 12 shows the fractional contribution of the vibrational frequencies to the spectra in fig. 3. We find that contributions from 6-membered C atom ring structures increase logarithmically with increasing film thickness. Raman spectra from the thinnest films contain a significant contribution from 5- and 7-membered rings. As a-C films grow in thickness to 50 nm, contribution from the 7-membered rings appears to decrease exponentially. Not until this contribution becomes negligible does the fraction of signal from 5-membered C rings begin to decrease. The deconvolution of the Raman spectra for films ranging from 100 to 200 nm in thickness are nearly identical.

The Raman deconvolutions shown in fig. 11 as a function of growth energy suggests that for the most diamondlike films, π-bonded carbon atoms are most likely to be present in stable 6-membered ring structures. However, the results in fig. 12 for a-C as a function of thickness finds that a combination of 5-, 6-, and 7-membered π-bonded ring topologies exist for the films with the highest densities. Since the energetic growth of a-C films is kinetically driven, thermodynamic equilibrium is not achieved. Otherwise, all films would consist of nanocrystalline graphite. In fact, kinetics would likely drive the development of ring structures that can be more readily squeezed into a very tight region. Planar 6-membered carbon ring topologies do not fit efficiently into a matrix of predominantly fourfold coordinated carbon atoms. Combinations of 5-, 6- and 7-membered carbon rings provide the greatest curvature.[19, 20]

The evolution of π-bonded ring topologies evidenced in fig. 12 can be related to the mass densities, shown in fig. 8, as a function of film thickness. Films with thicknesses $\leq$ 50 nm have density ~ 3.35 g/cm^3. These films also have a measurable fraction of 7-membered carbon ring topologies. It is worth noting that even a small presence of 7-membered rings in the films, inferred from the Raman deconvolutions, correlates with the measurement of very high density. Only with

the disappearance of this ring topology for film thicknesses > 50 nm does the density begin to significantly decrease. This is consistent with the density determinations for films grown as a function of PLD energy density where even relatively low growth energetics results in films with unexpectedly high mass densities. The Raman spectra deconvolutions shown in fig. 11 infer large fractions of 7-membered carbon rings. Therefore, despite what should be a significantly lower threefold coordinated carbon atom concentration, the curvature of π-bonded ring clusters allowed by the presence of large quantities of both 5- and 7-membered ring topologies improves the topographical packing density of these structures into the σ-bonded matrix.

Continuing the assumption that the use of these π-bonded ring vibrational frequencies is a valid description of the carbon Raman bands, several questions arise. First, why does the population of 7-membered C atom ring topologies decrease with film thickness up to 50 nm, while the 5-membered ring fraction remains constant? Second, why does the population of 5-membered carbon ring topologies decrease only after the disappearence of 7-membered carbon atom rings, for films somewhere between 50 – 100 nm? Third, why does an equilibrium of ring statistics occur for films $\geq$ 100 nm despite the continually decreasing mass density shown in fig. 8? And finally, are these π-bonded topological tendencies observed for films grown at constant energy as a function of film thickness consistent with the trends observed in fig. 11 for films of uniform thickness grown as a function of PLD energy density? This last question will be addressed in the context of each of the previous questions.

A significant presence of 5- and 7-membered π-bonded ring topologies occur under two completely different situations. The first is for a-C films grown at the lower PLD energy densities. These films have a greater fraction of π-bonded carbon atoms than films grown at higher energies. This is represented by their lower mass densities and higher optical absorbance. However, such films are still amorphous and grow in a highly-strained local environment. Hence, large flat sheets of 6-membered graphene rings do not co-exist in a matrix with amorphous 4-fold coordinated

carbon atoms. Clusters of π-bonded ring structures require curvature to achieve a high C atom packing density with the σ-bonded ring structures. This curvature is achievable using 5- and 7-membered rings, such as fragments of fullerene structures.

The second situation is at the opposite end of the growth spectrum. Films grown at high PLD energies with thickness ≤ 50 nm resulting in large mass density also contain significant amounts of 5- and 7-membered rings. In addition, a-C films < 20 nm thick do not have fully developed interfacial and surface regions. Depositing carbon species to the surface of these films are still affected by the presence of the silicon substrate. This environment is in a very high degree of localized strain; carbon species are essentially implanting from both the surface and from reflections off the substrate. This very energetic regime of film deposition leads to very constrained topographical regions for π-bonded topologies to even exist. Indeed, such films have two seemingly contradictory properties: a very high mass density and a very high optical absorption coefficient. Only by forming highly curved fullerene-like fragments can the packing of three- and fourfold coordinated carbon ring structures be optimized to result in a high mass density, even in the presence of additional π-bonded carbon atoms. This can account for both the high density and the high absorption in the thinnest films.

Indeed, it is worth noting that the density of films grown at 45 J/cm^2 do not begin to decrease below 3.35 g/cm^3 with increasing thickness until there is no longer a detectable Raman signature of 7-membered π-bonded ring topologies. Density sharply decreases for films > 50 nm thick, and the fraction of 5-membered π-bonded ring topologies also decreases to a constant value for films near 100 nm in thickness. The extinction of the 7-membered ring fraction occurring as a function of thickness before the 5-membered ring fraction even begins to decline suggests that the 5-membered π-bonded rings have a lower free energy, i.e. are thermodynamically more stable. Of course, the constant increase of the 6-membered ring fraction over the entire range of film thickness studied

demonstrates that this topology is the most energetically favorable, which is expected given that it represents the basis building block of graphite.

The real question that arises is why does the mass density decrease for films with thicknesses greater than those in which 7-membered π -bonded topologies are present? The answer must be related to the kinetic energy driven growth process of a-C and the existence of the very high 5 – 10 GPa residual stresses. It is widely believed that the high fourfold coordinated carbon content of a-C films is the result of the subplantation of energetic incident carbon species beneath a growing film surface. This leads to regions with very high localized pressure achieved through the creation of point defects.[54, 55] Indeed, the existence of these high film stresses results in spallation of films above a critical thickness from the substrate. Note that even a-C films grown using lower energy species resulting in lower mass density also have significant residual stresses of a few GPa. Ultimately, there is a limit on the ability to decrease the free energy of an a-C surface: all films above some critical thickness must, and do, delaminate. Therefore, an explanation for the density gradient in a-C films is in the ongoing competition between the surface free energy of a smooth film with the stress energy resulting from the growth process. As a film thickness increases during growth, the free energy of the surface must decrease to prevent spallation. Presumably this is accomplished with the evolution of an increasing fraction of higher stability π-bonded carbon atoms, and in particular, arranged mostly in 6-membered ring topologies. Apparently, as long as a significant portion of the threefold coordinated fraction consists of 5- and 7-membered rings, enough flexibility exists to accommodate an increasing fraction of π-bonded carbon atoms in a high density matrix. Once the 7-membered ring topologies are no longer being formed, the density begins to decrease.

At first glance, the relatively uniform 5- and 6-membered ring constitution of the π-bonded carbon fraction for films 100 – 200 nm thick appears inconsistent with a decreasing density over this region of growth. Clearly the decreasing mass density implies an increasing 3-fold

coordinated carbon atom population. The overall increase in the π-bonded fraction in the surface regions may generate the necessary free energy reduction to counter the stress energy. Furthermore, it is also possible that other forms of π-bonded carbon nanostructures are forming that are not detectable by Raman spectroscopy with excitation at 514 nm, such as conjugated chain structures. Note that the absorption coefficients shown fig. 4(c) also do not change appreciably over this range of thickness. Hence, it is plausible that the relative concentration of threefold coordinated carbon ring topologies does not change in this region of changing density.

The detailed analysis of the Raman spectra presented above provides a self-consistent interpretation for the evolution of threefold coordinated carbon ring topologies as a function of both growth energetics and thickness. Howver, there is currently no definitive evidence for the existence of such carbon nanostructures in a-C films.

V. CONCLUSIONS

We provide a description of threefold coordinated π-bonded carbon topologies that exist in amorphous carbon films based upon detailed analyses from both Raman and x-ray reflectivity spectra. Mass density increases with increasing growth energy (at least over the range of growth energetics accessible with our PLD apparatus), and decreases with increasing thickness (or distance from the substrate). The very high 3.35 g/cm^3 densities determined for the thinnest films are consistent with the results of previous analysis. A simple model is presented describing an thermodynamic driving force between competing factors: (1) the free energy of topographical clusters of π-bonded topologies, and (2) the energy of residual film stress. Briefly, deposition kinetics dominate the early stages of a-C film growth, resulting in metastable bonding topologies. As film thickness increases, the energy resulting from the high residual stresses forces the formation of more energetically favorable π-bonded graphene topologies. Since the topographical clustering of bonding topologies is essentially quenched during growth, there is negligible effect on the underlying film. This provides considerable forces for newly grown film material to form

more energetically favorable bonding topologies, leading to a topographical gradient of bonding topologies through the thickness of an a-C film.

ACKNOWLEDGEMENT

This work was supported in part by Sandia National Laboratories, US DOE under contract No. DE-ACO4-94AL85000 and from the NSF under grant DMR93-13047. We would like to thank T. Thurston and B. M. Ocko for the use of beamline X22A at the NSLS, T. A. Friedmann for providing some a-C films, and J. P. Sullivan, P. A. Schultz and E. B. Stechel for discussions with valuable insight.

REFERENCES

1. S. Kasi, H. Kang, and J. W. Rabalais, Phys. Rev. Lett. **59**, 75 (1987).
2. S. S. Wagal, E. M. Juengerman, and C. B. Collins, Appl. Phys. Lett. **53**, 187 (1988).
3. P. J. Martin, S. W. Filipczuk, R. P. Netterfield, J. S. Field, D. F. Whitnall, and D. R. McKenzie, J. Mater. Sci. Lett. **7**, 410 (1988).
4. J. Robertson, Phys. Rev. Lett. **68**, 220 (1992).
5. V. I. Merkulov, J. S. Lannin, C. H. Munro. S. A. Asher, V. S. Veerasamy, and W. I. Milne, Phys. Rev. Lett. **78**, 4869 (1997).
6. R. Lossy, D. L. Pappas, R. A. Roy, J. J. Cuomo, and V. M. Sura, Appl. Phys. Lett. **61**, 161 (1992).
7. N. Missert, T. A. Friedmann, J. P. Sullivan, and R. G. Copeland, Appl. Phys. Lett. **70**, 1995 (1997).
8. B. S. Satyanarayana, A. Hart, W. I. Milne, and J. Robertson, Appl. Phys. Lett. **71**, 1430 (1997).
9. J. E. Jaskie, MRS Bulletin, **21**, 59 (1996).
10. J. P. Sullivan, T. A. Friedmann, A. J. Magerkurth, M. P. de Boer, M. M. Bridges, and C. I. H. Ashby, Abstracts of the 1998 Fall Materials Research Society Meeting, p. 502 (1998).
11. P. C. Kelires, Phys. Rev. Lett. **68**, 1854 (1992).
12. P. C. Kelires, Phys. Rev. B **47**, 1829 (1993).
13. P. C. Kelires, Phys. Rev. Lett. **73**, 2460 (1994).
14. Th. Frauenheim, P. Blaudeck, U. Stephan, and G. Jungnickel, Phys. Rev. B **48**, 4823 (1993).
15. C. Z. Wang and K. M. Ho, Phys. Rev. Lett. **71**, 1184 (1993).
16. D. A. Drabold, P. A. Fedders, and P. Stumm, Phys. Rev. B **49**, 16415 (1994).
17. N. A. Marks, D. R. McKenzie, B. A. Pailthorpe, M. Bernasconi, and M. Parrinello, Phys. Rev. Lett. **76**, 768 (1996).

18. P. A. Schultz and E. B. Stechel, Phys. Rev. B **57**, 3295 (1998).

19. J. K. Walters, K. W. R. Gilkes, J. D. Wicks, and R. J. Newport, Phys. Rev. B **58**, 8267 (1998).

20. J. Dong and D. A. Drabold, Phys. Rev. B **57**, 15591 (1998).

21. M. P. Siegal, J. C. Barbour, P. N. Provencio, D. R. Tallant, and T. A. Friedmann, Appl. Phys. Lett. **73**, 759 (1998).

22. C. A. Davis, G. A. J. Amaratunga, and K. M. Knowles, Phys. Rev. Lett. **80**, 3280 (1998).

23. D. A. Drabold, P. A. Fedders, and M. P. Grumbach, Phys. Rev. B **54**, 5480 (1996).

24. D. L. Pappas, K. L. Saenger, J. Bruley, W. Krakow, J. J. Cuomo, T. Gu, and R. W. Collins, J. Appl. Phys. **71**, 5675 (1992).

25. M. P. Siegal, T. A. Friedmann, S. R. Kurtz, D. R. Tallant, R. L. Simpson, F. Dominguez, and K. F. McCarty, Mater. Res. Soc. Symp. Proc. **349**, 507 (1994).

26. H. C. Ong and R. P. H. Chang, Phys. Rev. B **55**, 13213 (1997).

27. D. R. Tallant, J. E. Parmeter, M. P. Siegal, and R. L. Simpson, Diamond and Related Mater. **4**, 191 (1995).

28. Y. Wang, D. C. Alsmeyer, and R. L. McCreery, Chem. Mater. **2**, 5567 (1990).

29. D. R. Tallant, T. A. Friedmann, N. A. Missert, M. P. Siegal, and J. P. Sullivan, Mater. Res. Soc. Symp. Proc. **498**, 37 (1998).

30. Y. Huai, M. Chaker, J. N. Broughton, E. Gat, H. Pepin, T. Gu, X. Bian, and M. Sutton, Appl. Phys. Lett. **65**, 830 (1994).

31. M. F. Toney and S. Brennan, J. Appl. Phys. **66**, 1861 (1989).

32. M. F. Toney, T. C. Huang, S. Breenan, and Z. Rek, J. Mater. Res. **3**, 351 (1988).

33. L. J. Martinez-Miranda et al, (unpublished).

34. K. W. R. Gilkes, H. S. Sands, D. N. Batchelder, J. Robertson, and W. I. Milne, Appl. Phys. Lett. **70**, 1980 (1997).

35. J. J. Cuomo, D. L. Pappas, J. Bruley, J. P. Doyle, and K. L. Saenger, J. Appl. Phys, **70**, 1706 (1991).

36. G. Adamopoulos, K. W. R. Gilkes, J. Robertson, N. M. J. Conway, B. Y. Kleinsorge, A. Buckley, and D. N. Batchelder, Diamond and Related Mater. **8**, 541 (1999).

37. R. L. C. Wu, A. K. Rai, A. Garscadden, P. Kee, H. D. Desai, and K. Miyoshi, J. Appl. Phys. **72**, 110 (1992).

38. G. Compagnini and G. Foti, Mater. Res. Soc. Symp. Proc, **498**, 89 (1998).

39. L. J. Martinez-Miranda, J. P. Sullivan, T. A. Friedmann, M. P. Siegal, T. W. Mercer, and N. J. DiNardo, Mater. Res. Soc. Symp. Proc. **383**, 459 (1995).

40. P. H. Gaskell, A. Saeed, P. Chieux, and D. R. McKenzie, Phys. Rev. Lett. **67**, 1286 (1991).

41. F. Xiong, Y. Y. Wang, V. Leppert, and R. P. H. Chang, J. Mater. Res. **8**, 2265 (1993).

42. J. Kulik, Y. Lifshitz, G. D. Lempert, J. W. Rabalai, and D. Marton, J. Appl. Phys. **76**, 5063 (1994).

43. E. Grossman, G. D. Lempert, J. Kulik, D. Marton, J. W. Rabalais, and Y. Lifshitz, Appl. Phys. Lett. **68**, 1214 (1996).

44. Z. Y. Chen, Y. H. Yu, J. P. Zhao, X. Wang, X. H. Liu, and T. S. Shi, J. Appl. Phys. **83**, 1281 (1998).

45. G. H. Vineyard, Phys. Rev. B, **26**, 4146 (1982).

46. T. A. Friedmann, K. F. McCarty, J. C. Barbour, M. P. Siegal, and D. C. Dibble, Appl. Phys. Lett. **68**, 1643 (1996).

47. M. Nakamizo, R. Kammereck, and P. L. Walker, Jr., Carbon, **12**, 259 (1974).

48. F. Tuinstra and J. L. Koenig, J. Chem. Phys. **53**, 1126 (1970).

49. T. E. Doyle and J. R. Dennison, Phys. Rev. B **51**, 196 (1995).

50. J. P. Sullivan and T. A. Friedmann, in *Amorphous Carbon: State of the Art,* edited by S. R. P. Silva, J. Robertson, W. I. Milne, and G. A. J. Amaratunga, (World Scientific, Singapore, 1998), pp. 281-295.

51. J. P. Sullivan, T. A. Friedmann, R. G. Dunn, E. B. Stechel, P. A. Schultz, M. P. Siegal, and N. Missert, Mater. Res. Soc. Symp. Proc. **498**, 97 (1998).

52. W. F. Maddams, American Laboratory, p. 59 (March 1986).

53. M. P. Siegal, L. J. Martinez-Miranda, N. J. DiNardo, D. R. Tallant, J. C. Barbour, and P. N. Provencio, Proc. of SPIE, **3343**, 885 (1998).

54. Y. Lifshitz, S. R. Kasi, and J. W. Rabelais, Phys. Rev. Lett. **62**, 1290 (1989).

55. D. R. McKenzie, D. Muller, and B. A. Pailthorpe, Phys. Rev. Lett. **67**, 773 (1991).

Figure Captions

1. Normalized Raman spectra for nominally 100 nm thick a-C films grown at PLD energy densities ranging from 5 – 125 J/cm^2.
2. Optical properties at 514.5 nm for nominally 100 nm thick films as a function of growth energetics determined from the integrated Raman peaks of Si both through an a-C film and on an exposed portion of the substrate. (a) Optical transparency; and (b) optical absorbance.
3. Normalized Raman spectra for a-C films grown using a constant PLD energy density of 45 J/cm^2 with thicknesses ranging from 5 – 200 nm.
4. Optical properties at 514.5 nm for a-C grown using a constant PLD energy density of 45 J/cm^2 as a function of film thickness. (a) Optical transparency; (b) optical absorbance; and (c) the optical absorption coefficient.
5. Normalized Raman spectra for 7 nm thick a-C films grown simultaneously on bare Si and on W-coated Si. The difference spectrum shows evidence of the 1450 cm^{-1} Raman vibration for C-C bonds in a-SiC.
6. X-ray reflectivity spectra for nominally 50 nm thick films grown using different PLD energy densities. The arrows note the presence of an unidentified Bragg scattering peak.
7. Mass density of a-C films grown vs. PLD energy density. The closed circles are from the analysis of the XRR spectra shown in fig. 6 and are compared with the open circles, measurements using RBS and TEM presented in ref. [Siegal 1]. The diamonds are densities measured for 100 nm thick films using XRR.
8. Mass density of a-C films grown at 45 J/cm^2 vs. film thickness from XRR spectra.
9. (a) The penetration depth of x-rays versus incident angle near the critical angle of reflection for a-C films with various densities. (b) Penetration depth at the critical angle of reflection versus a-C film density, extracted from the depth plots in (a), and hence, discretely calculated. The dashed line simply provides a guide for the eye.

10. Deconvolution of Raman spectra using the vibrational frequencies of idealized 5-, 6-, and 7-membered π-bonded topologies for 100 nm thick a-C film grown using a PLD energy density of (a) 125 J/cm^2; and (b) 5 J/cm^2. Note that the high-density film spectra can be fit using only the frequencies from relatively isolated 6-membered rings, while all of the available frequencies are required to fit the low-density film spectra.
11. The fraction of the carbon Raman band resulting from 5-, 6-, and 7-membered π-bonded ring topologies in 100 nm thick films as a function of growth energetics.
12. The fraction of the carbon Raman band resulting from 5-, 6-, and 7-membered π-bonded ring topologies in a-C grown using 45 J/cm^2 as a function of film thickness.

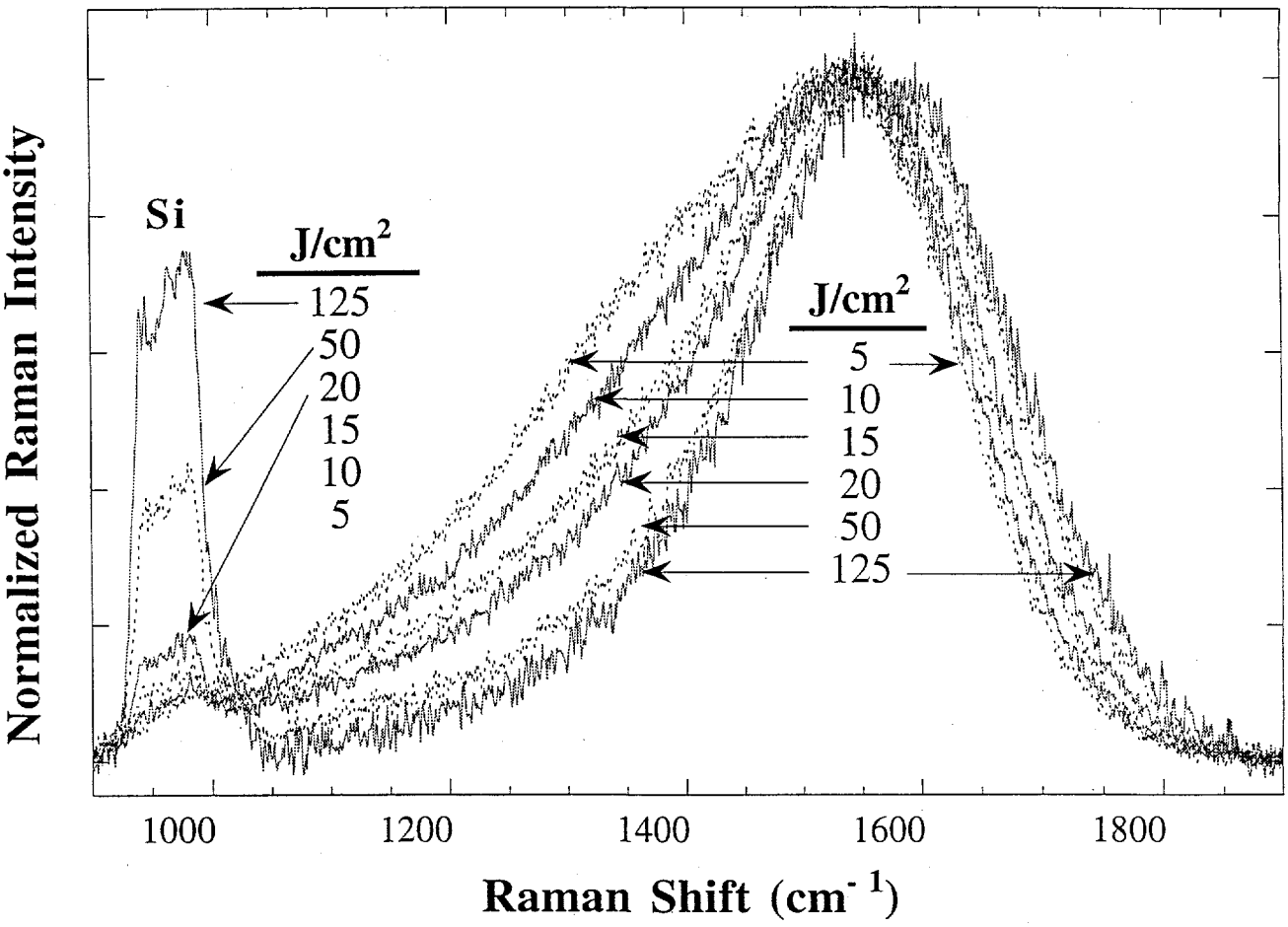
Normalized Raman Intensity
Si
J/cm2
125
50
20
15
10
5
J/cm2
5
10
15
20
50
125
1000
1200
1400
1600
1800
Raman Shift (cm-1)

Fig. 1

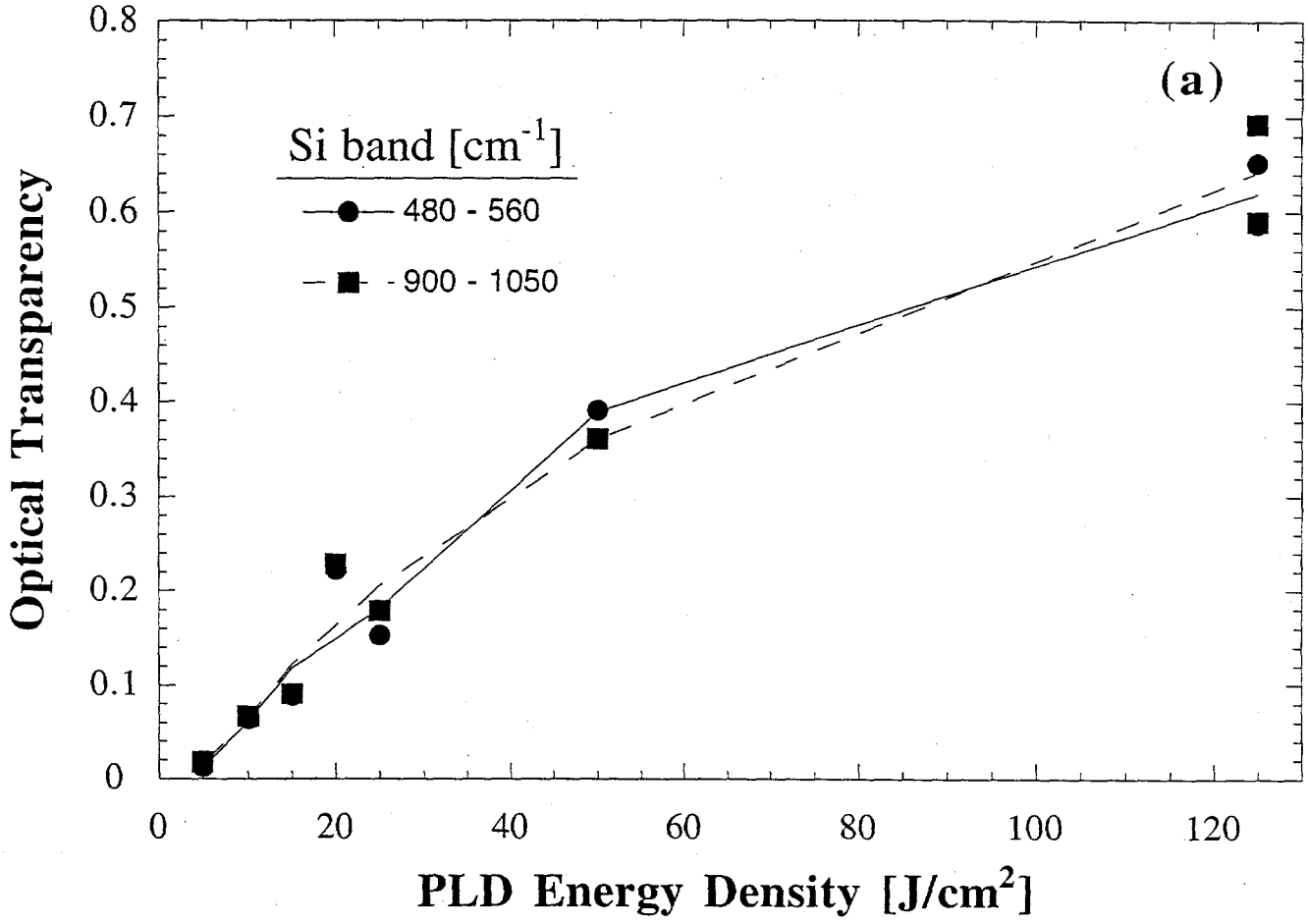
(a)
Si band [cm-1]
480 - 560
900 - 1050
Optical Transparency
PLD Energy Density [J/cm2]
0
0.1
0.2
0.3
0.4
0.5
0.6
0.7
0.8
0
20
40
60
80
100
120

Fig. 2a

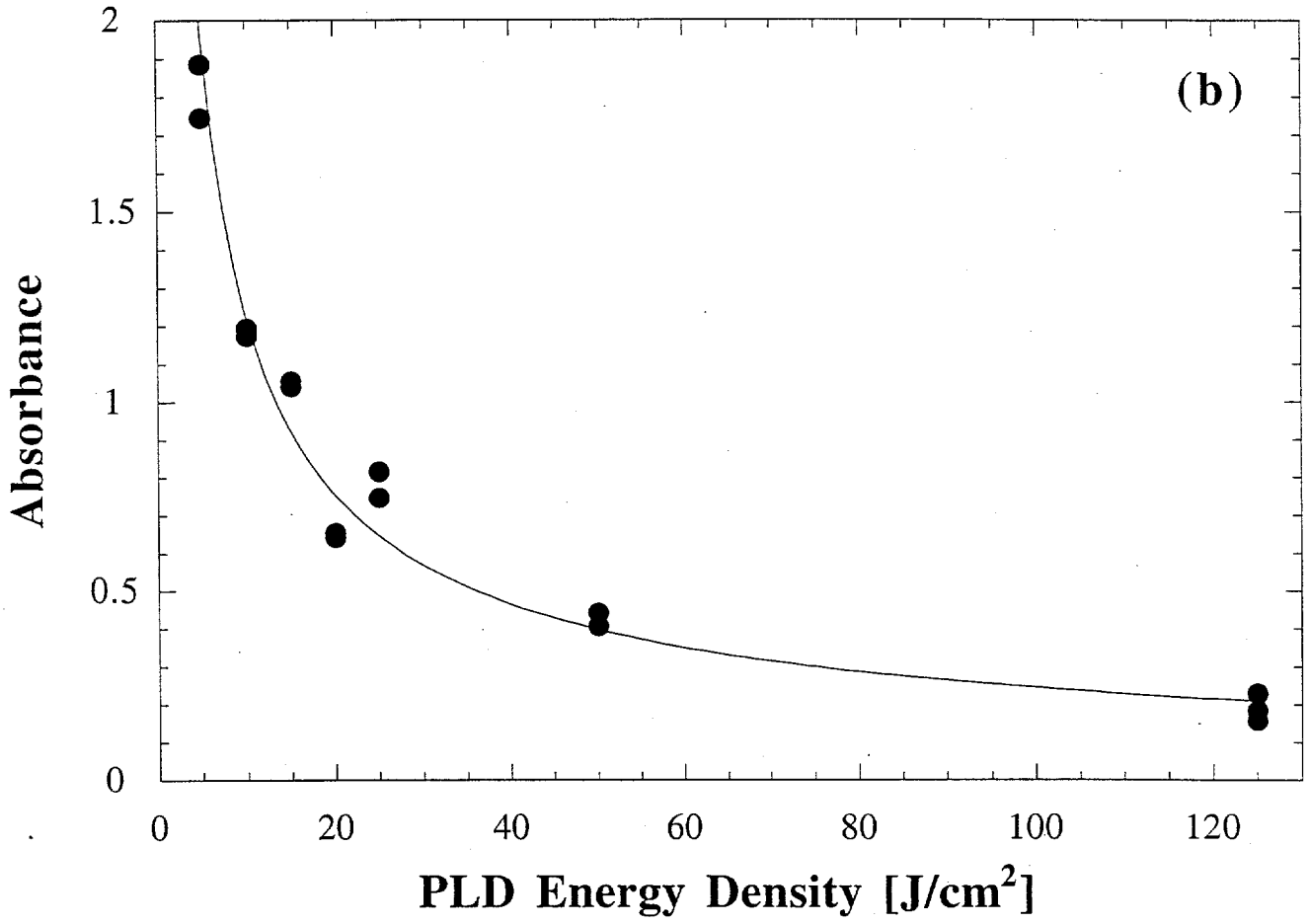
(b)
Absorbance
2
1.5
1
0.5
0
0
20
40
60
80
100
120
PLD Energy Density [J/cm^2]

Fig. 2b

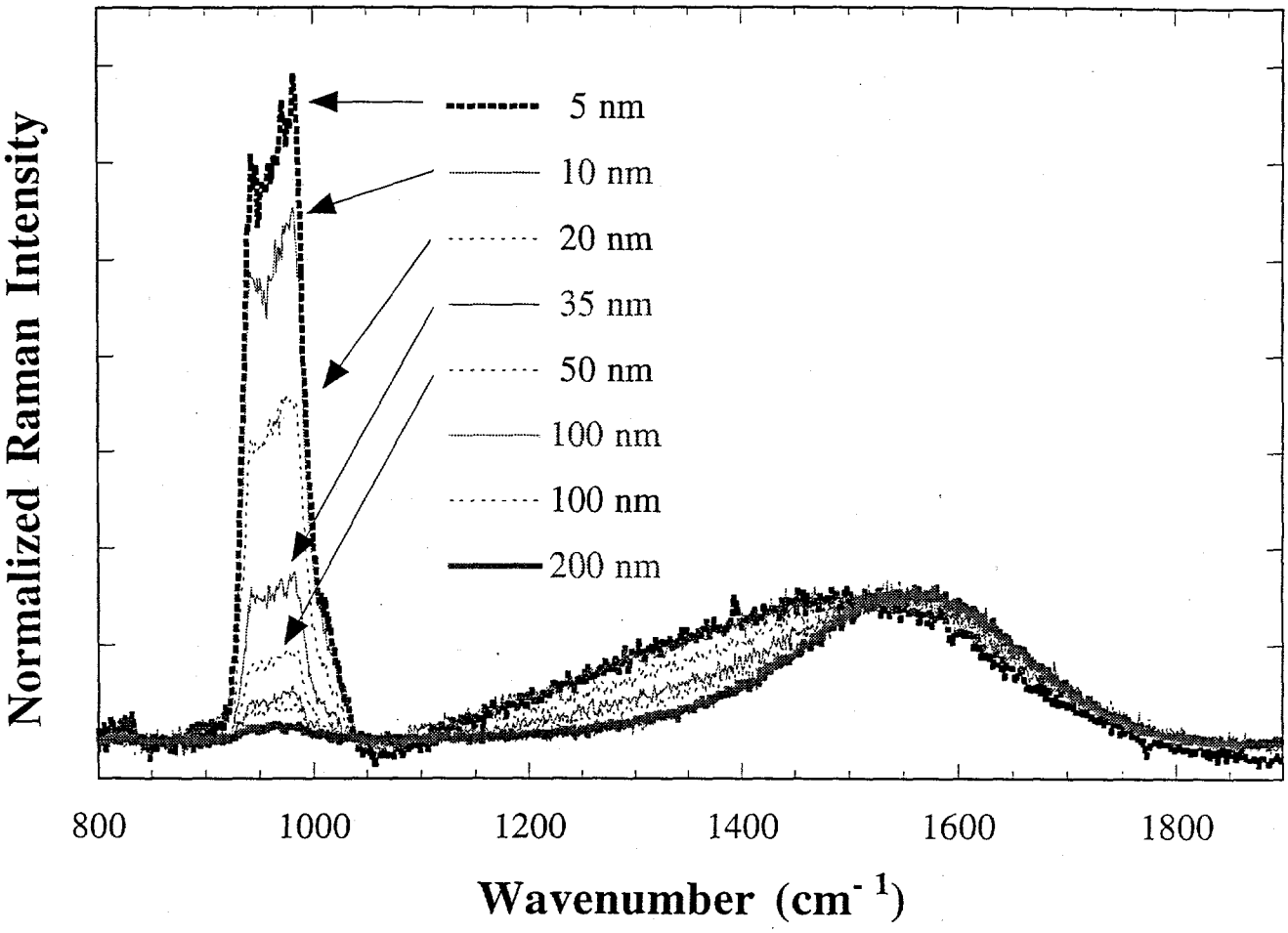
Normalized Raman Intensity
5 nm
10 nm
20 nm
35 nm
50 nm
100 nm
100 nm
200 nm
800
1000
1200
1400
1600
1800
Wavenumber (cm-1)

Fig. 3

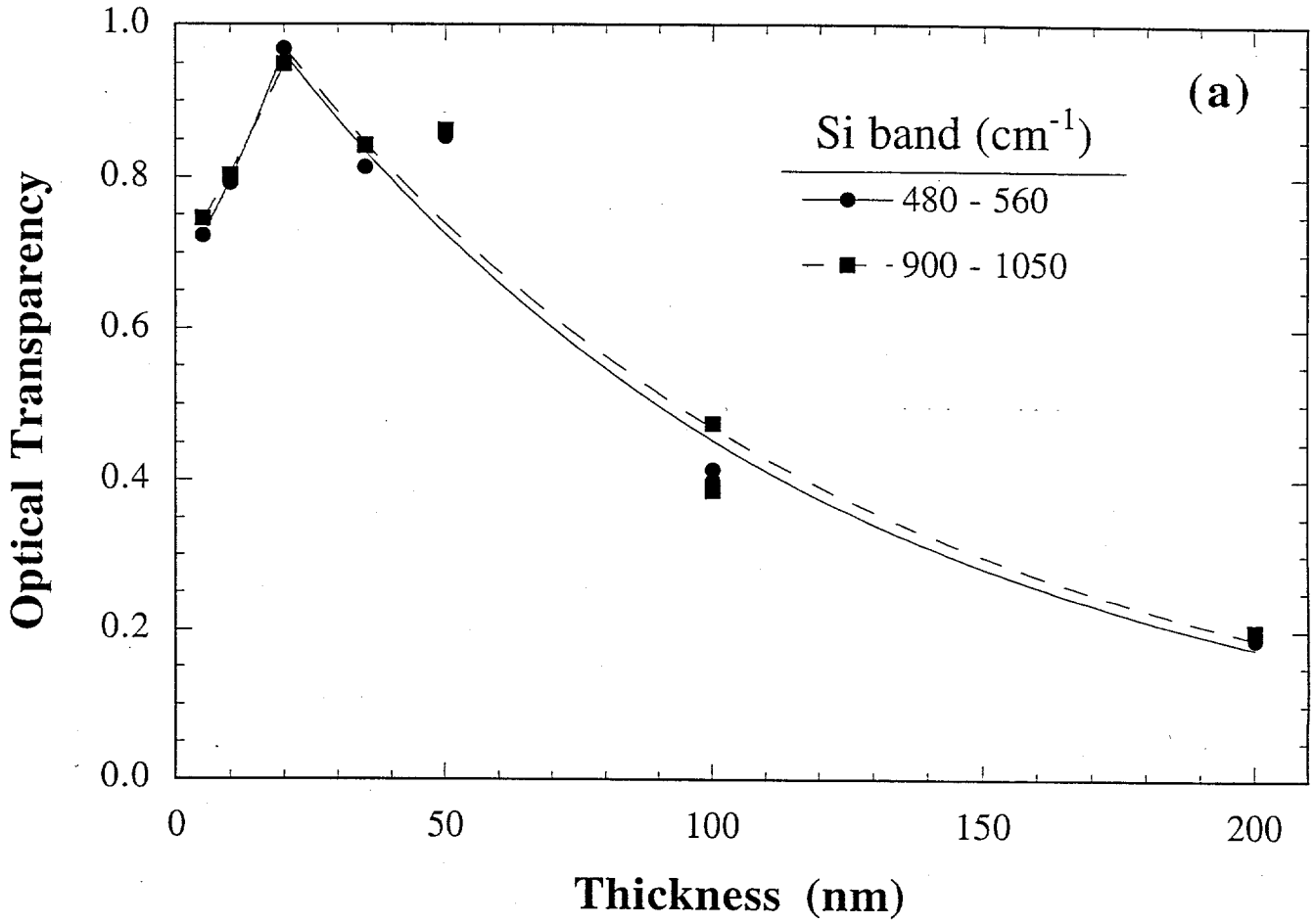
(a)
Si band (cm-1)
480 - 560
900 - 1050
Optical Transparency
Thickness (nm)
1.0
0.8
0.6
0.4
0.2
0.0
0
50
100
150
200

Fig 4a

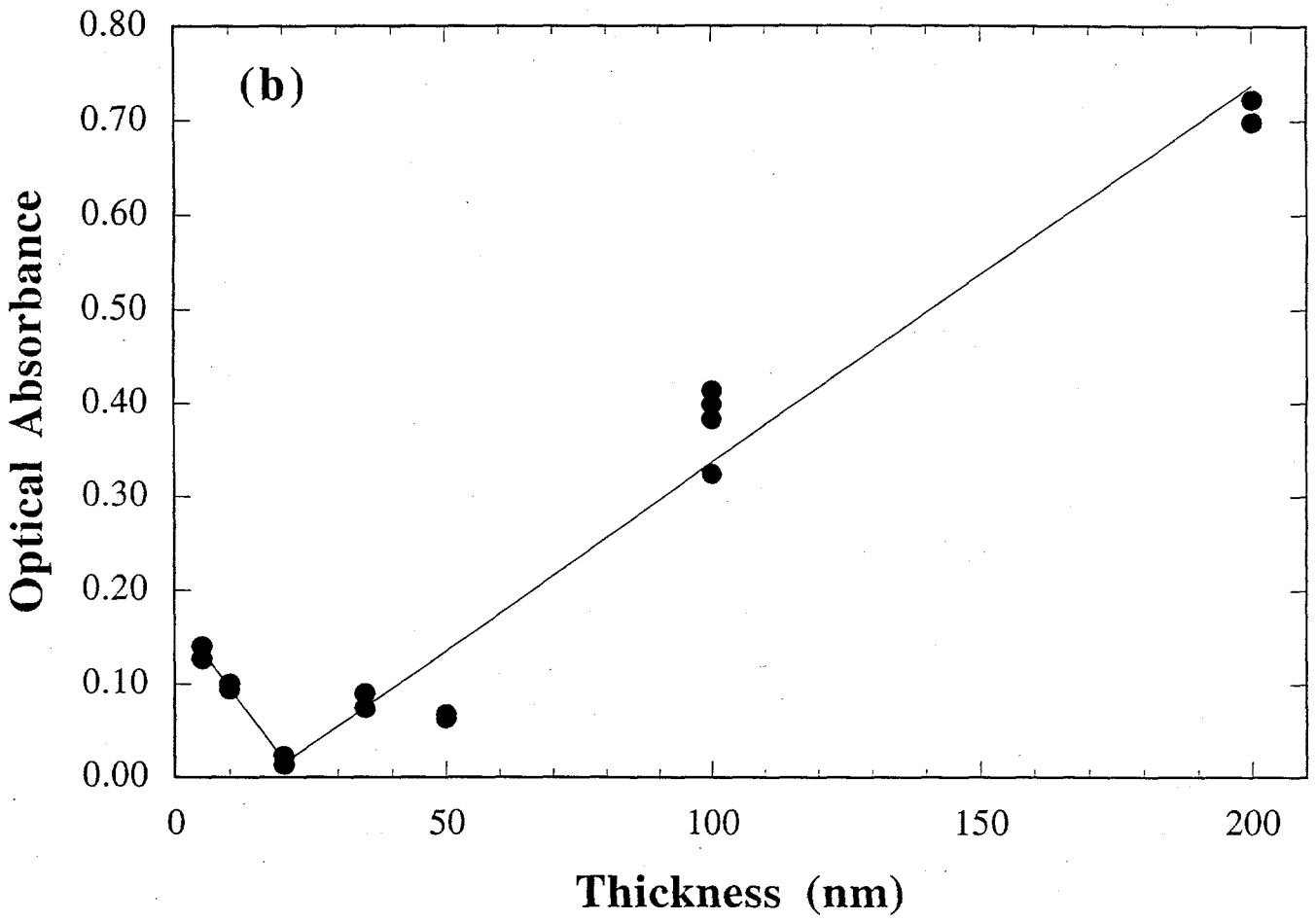
(b)
Optical Absorbance
0.80
0.70
0.60
0.50
0.40
0.30
0.20
0.10
0.00
0
50
100
150
200
Thickness (nm)

Fig. 4b

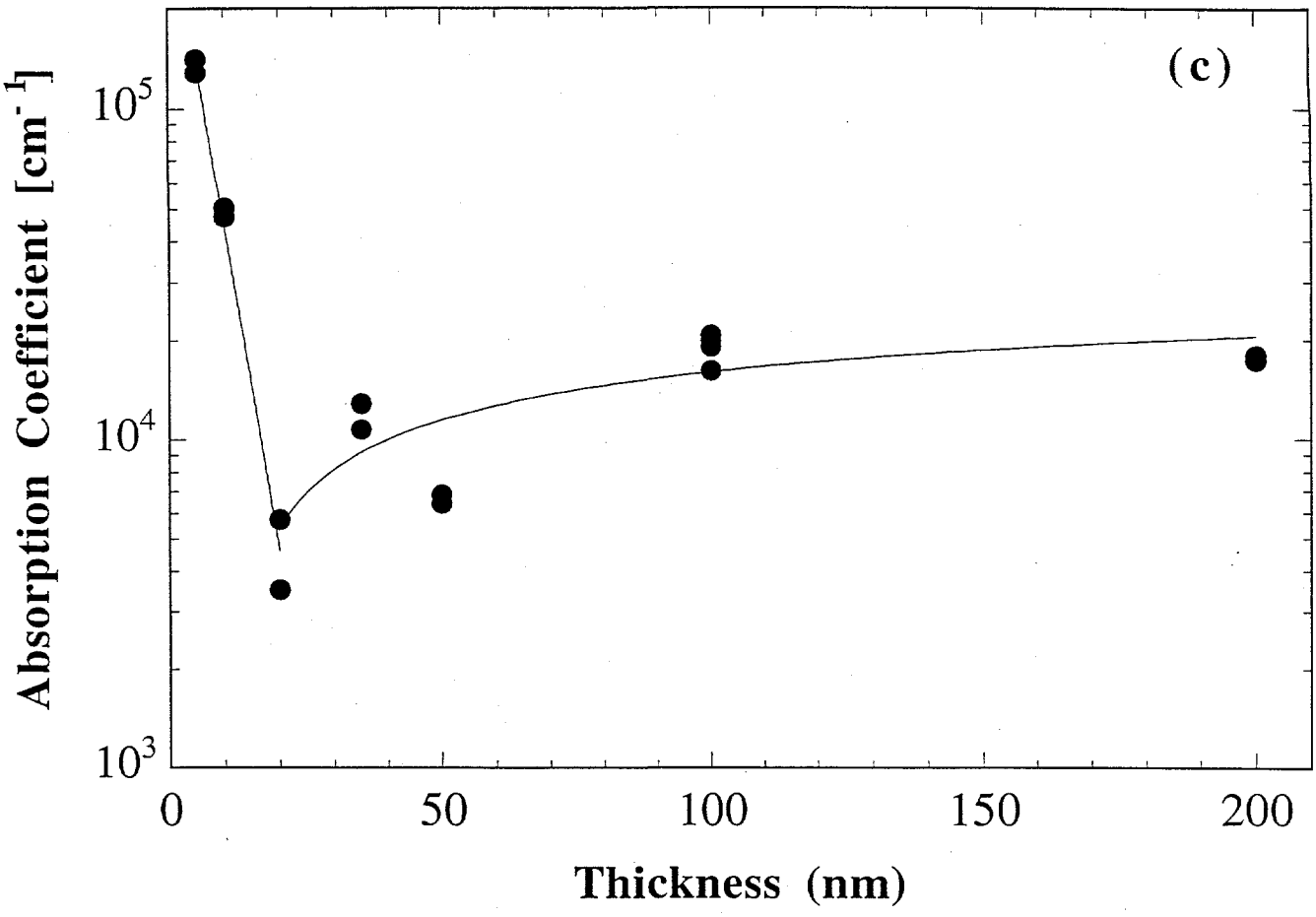
(c)
Absorption Coefficient [cm^{-1}]
10^5
10^4
10^3
0
50
100
150
200
Thickness (nm)

Fig. 4c

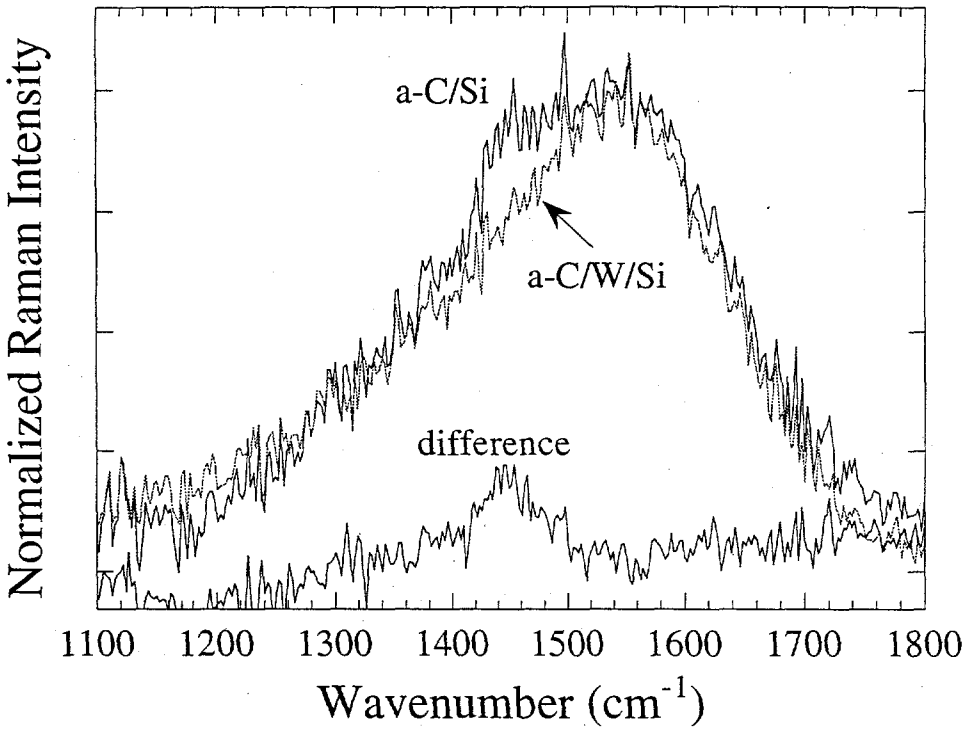
Normalized Raman Intensity
a-C/Si
a-C/W/Si
difference
1100
1200
1300
1400
1500
1600
1700
1800
Wavenumber (cm-1)

Fig. 5

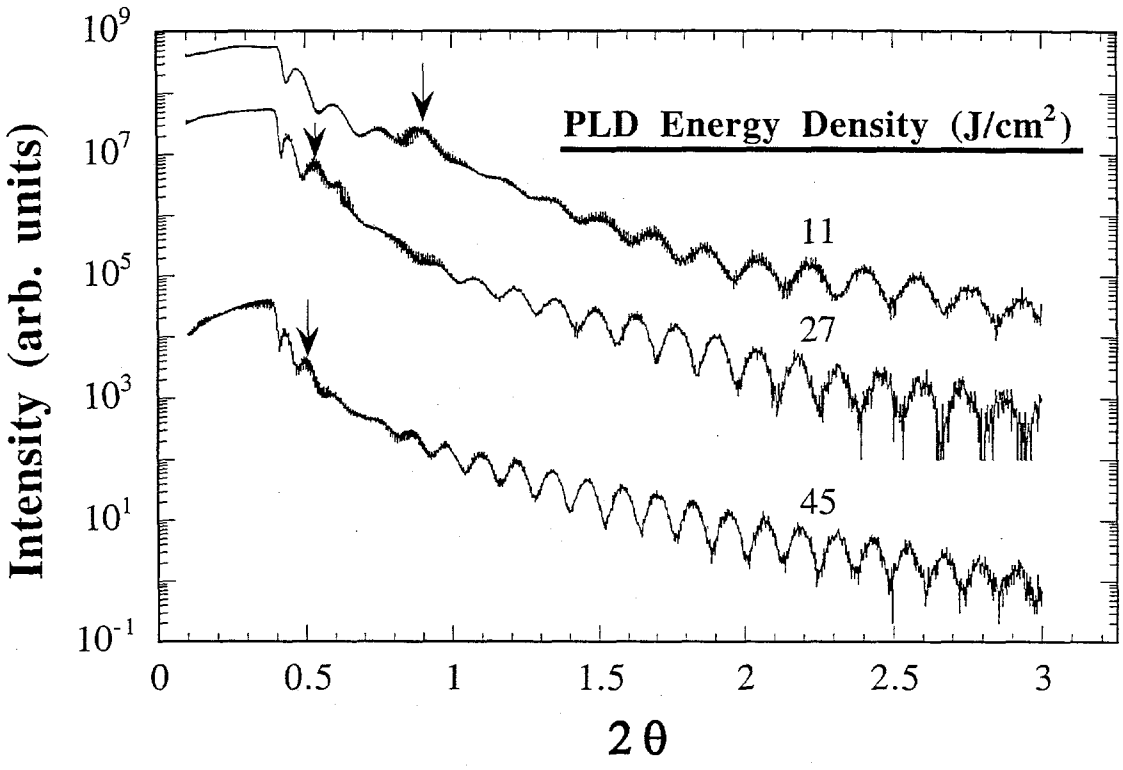
Intensity (arb. units)
10^9
10^7
10^5
10^3
10^1
10^{-1}
PLD Energy Density (J/cm^2)
11
27
45
0
0.5
1
1.5
2
2.5
3
2θ

Fig. 6

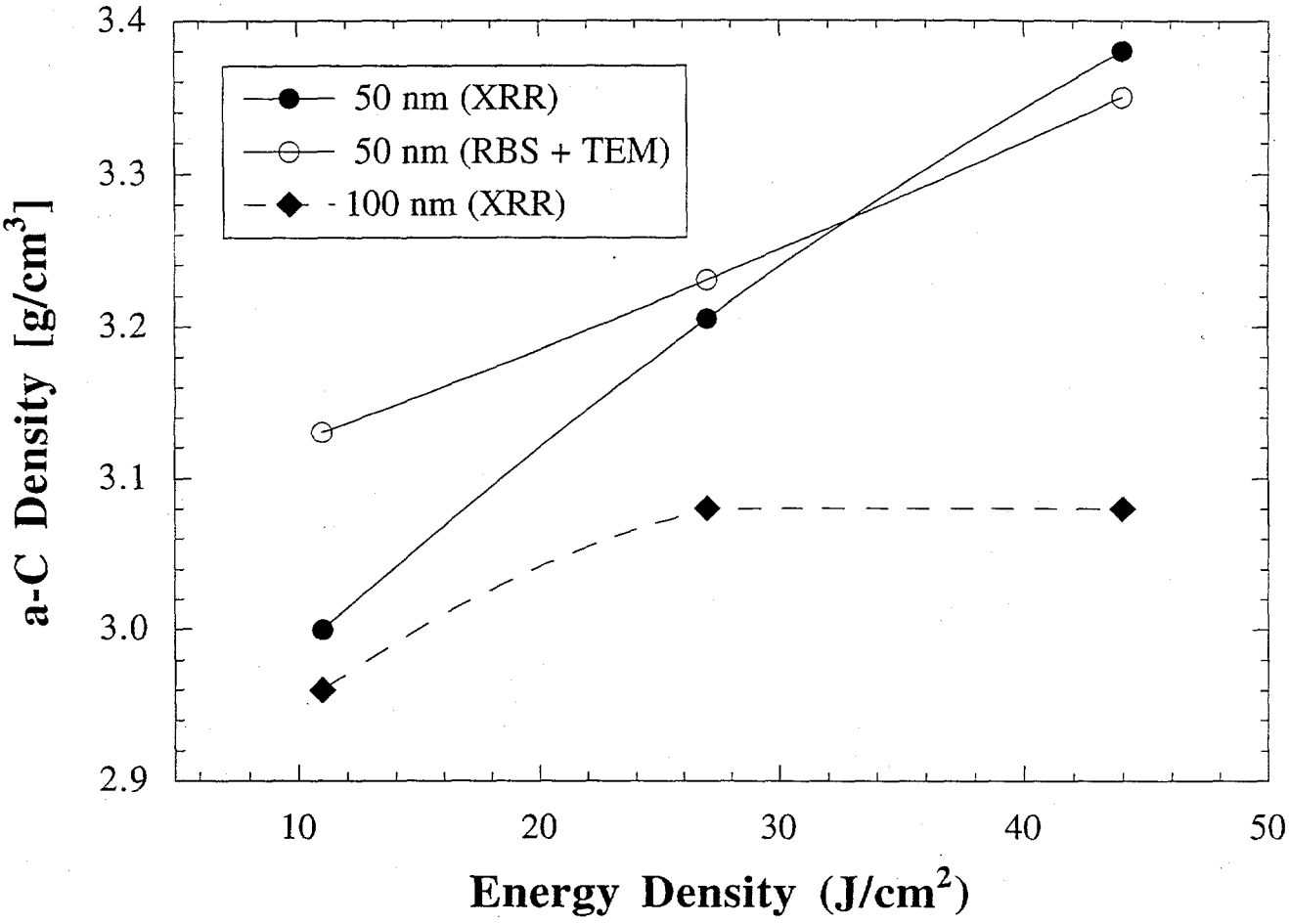
3.4
3.3
3.2
3.1
3.0
2.9
a-C Density [g/cm^3]
50 nm (XRR)
50 nm (RBS + TEM)
100 nm (XRR)
10
20
30
40
50
Energy Density (J/cm^2)

Fig. 7

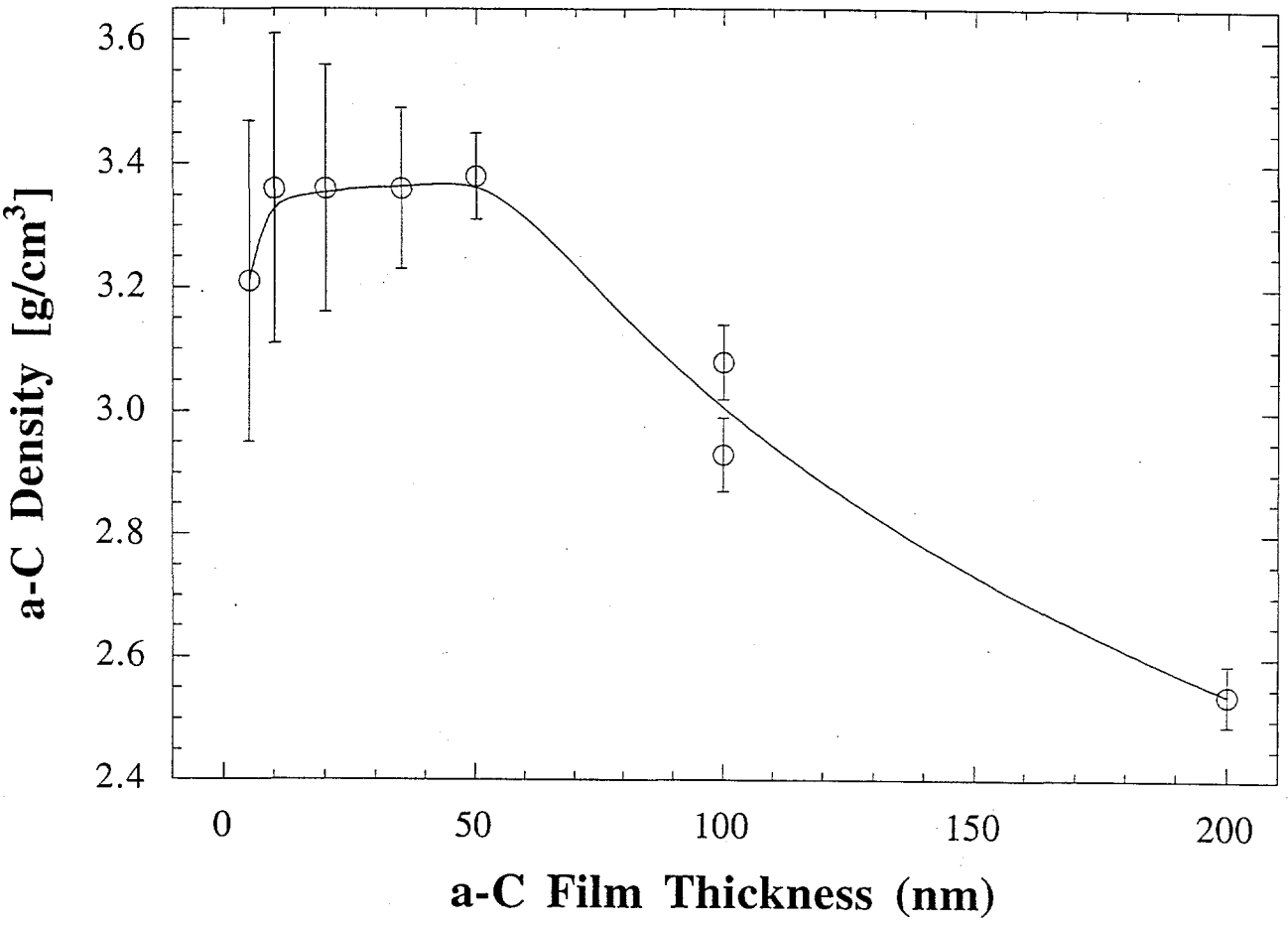
a-C Density [g/cm^3]
3.6
3.4
3.2
3.0
2.8
2.6
2.4
0
50
100
150
200
a-C Film Thickness (nm)

Fig. 8

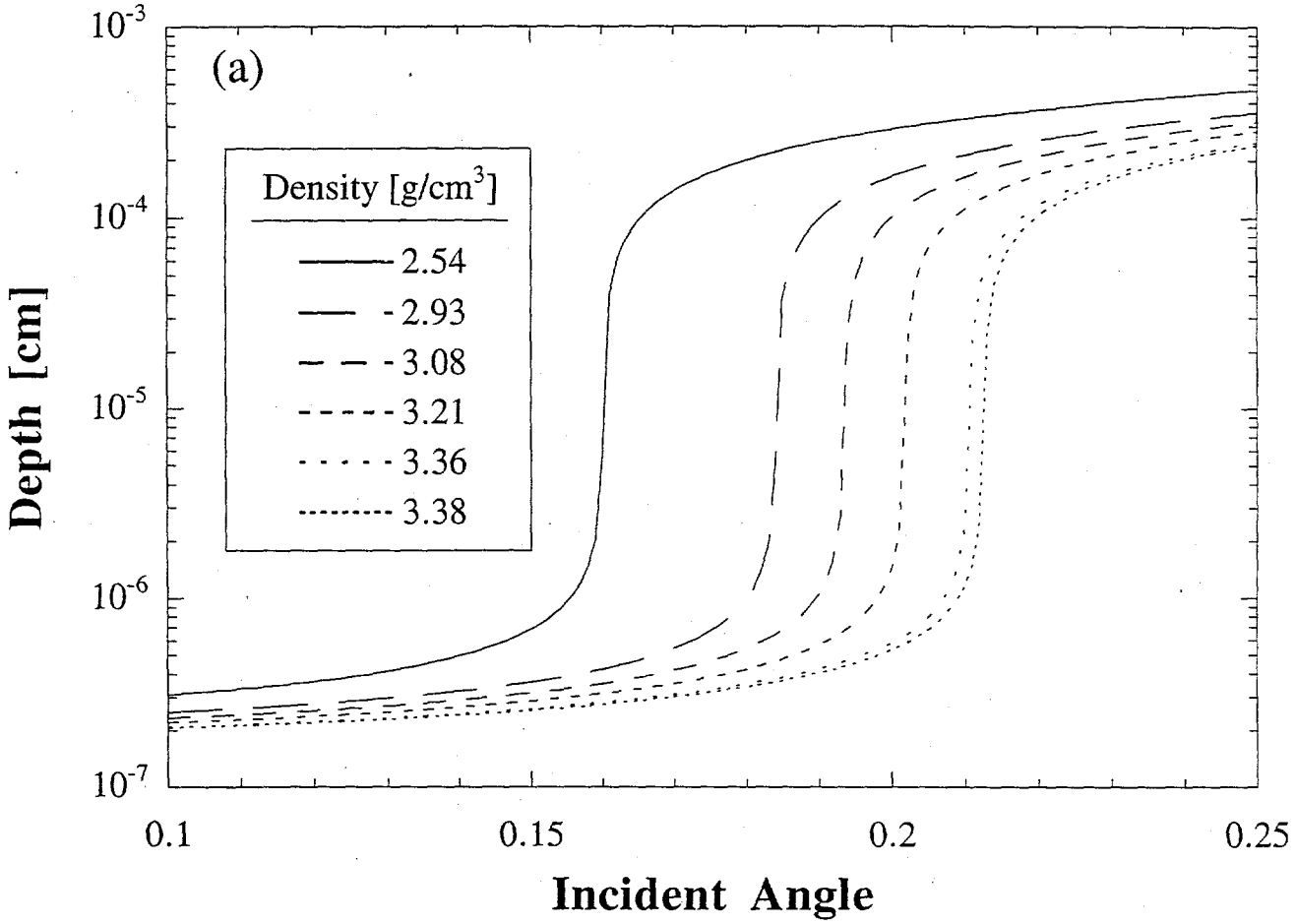
(a)
Density [g/cm3]
2.54
2.93
3.08
3.21
3.36
3.38
Depth [cm]
10-3
10-4
10-5
10-6
10-7
0.1
0.15
0.2
0.25
Incident Angle

Fig. 9a

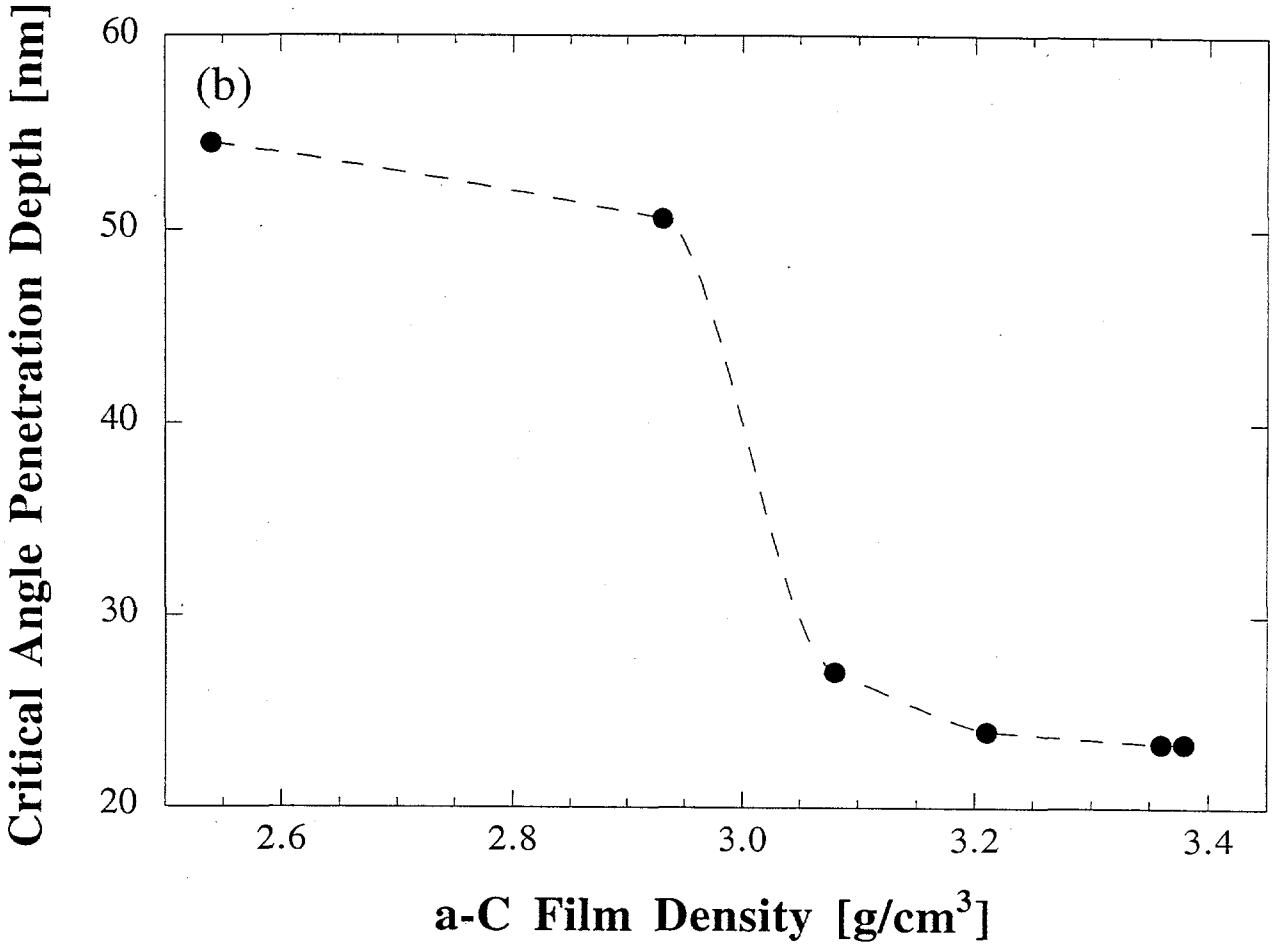
(b)
Critical Angle Penetration Depth [nm]
60
50
40
30
20
2.6
2.8
3.0
3.2
3.4
a-C Film Density [g/cm^3]

Fig. 9b

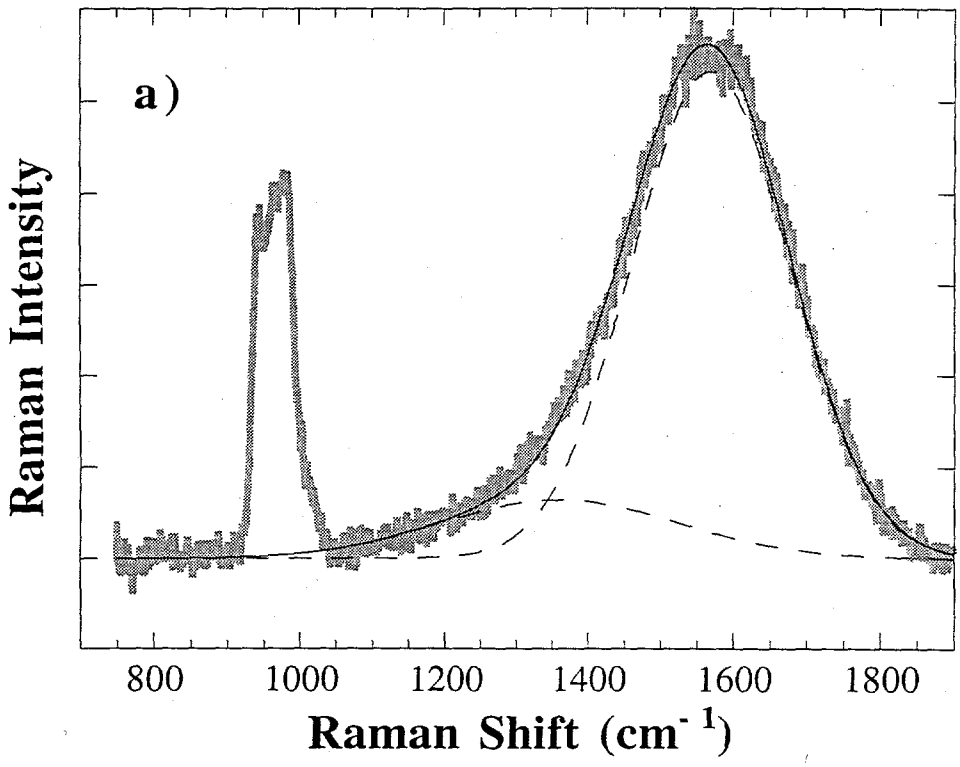
a)
Raman Intensity
800
1000
1200
1400
1600
1800
Raman Shift (cm^{-1})

Fig. 10 a

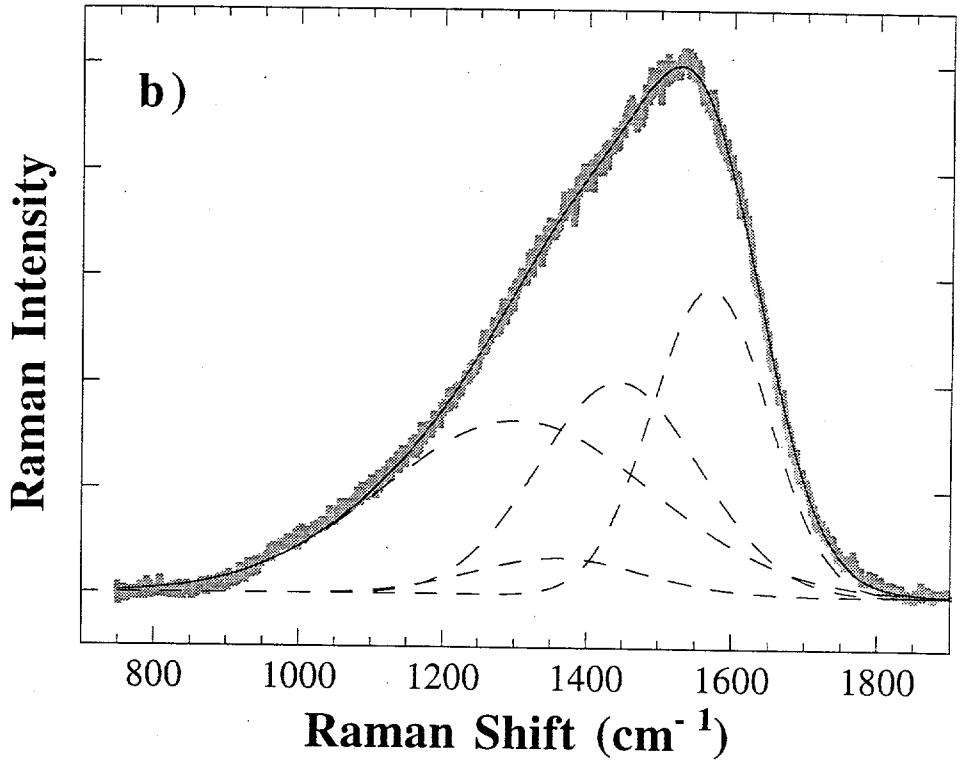
b)
Raman Intensity
800
1000
1200
1400
1600
1800
Raman Shift (cm-1)

Fig. 10b

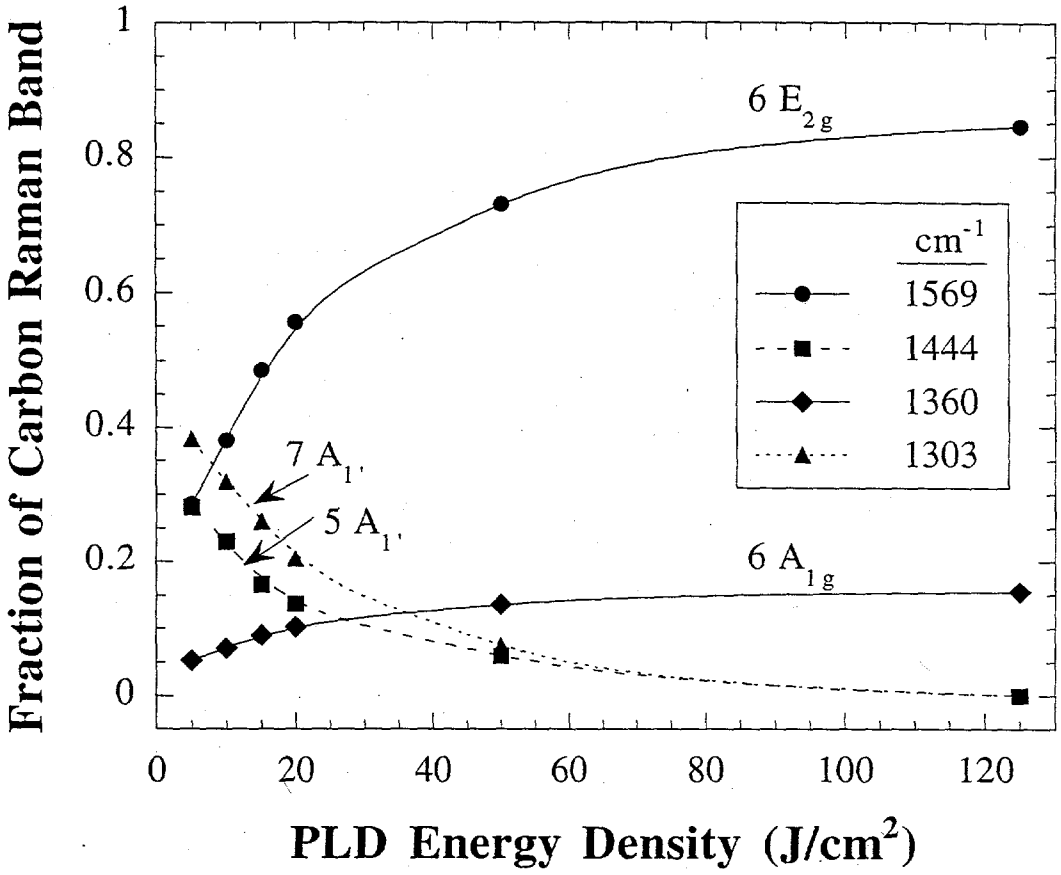
Fraction of Carbon Raman Band
1
0.8
0.6
0.4
0.2
0
0
20
40
60
80
100
120
PLD Energy Density (J/cm²)
6 E2g
7 A1'
5 A1'
6 A1g
cm-1
1569
1444
1360
1303

Fig. 11

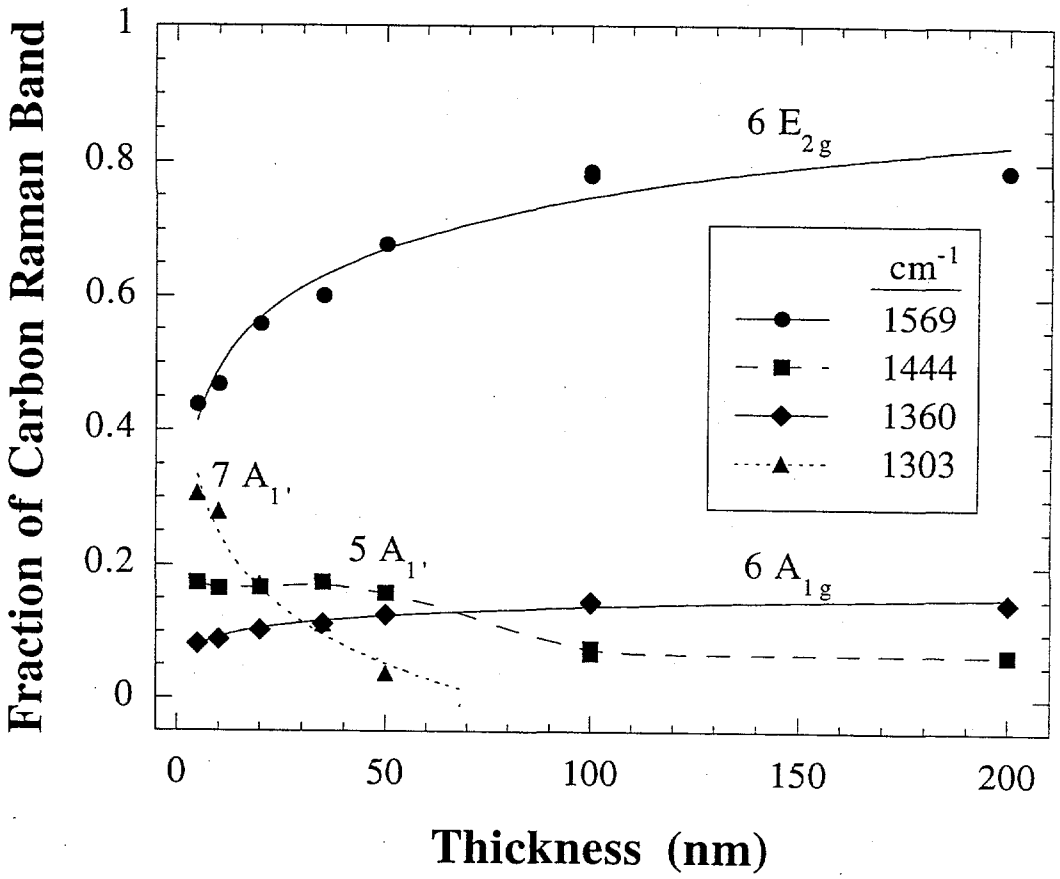
Fraction of Carbon Raman Band
1
0.8
0.6
0.4
0.2
0
0
50
100
150
200
Thickness (nm)
6 E2g
7 A1'
5 A1'
6 A1g
cm-1
1569
1444
1360
1303

Fig. 12